Key Points:
- Apollo basalt 12017 has a glass rind with an age <7 Ma old
- The 12017 glass has little or no stable natural remanent magnetization
- There is no robust paleomagnetic evidence for a lunar dynamo after ~3.56 Ga

Magnetism of a very young lunar glass

Jennifer Buz[1,2], Benjamin P. Weiss[1,3], Sonia M. Tikoo[3,4], David L. Shuster[3,4], Jérôme Gattacceca[5], and Timothy L. Grove[1]

[1]Department of Earth, Atmospheric, and Planetary Sciences, Massachusetts Institute of Technology, Cambridge, Massachusetts, USA, [2]Now at Division of Geological and Planetary Sciences, California Institute of Technology, Pasadena, California, USA, [3]Department of Earth and Planetary Science, University of California, Berkeley, California, USA, [4]Berkeley Geochronology Center, Berkeley, California, USA, [5]CNRS, Aix-Marseille Université, CEREGE UM 34, Aix-en-Provence, France

Abstract Recent paleomagnetic studies of Apollo samples have established that a core dynamo existed on the Moon from at least 4.2 to 3.56 billion years (Ga). Because there is no lunar dynamo today, a longstanding mystery has been the origin of magnetization in very young lunar samples (<~200 million years old (Ma)). Possible sources of this magnetization include transient fields generated by meteoroid impacts, remanent fields from nearby rocks magnetized during an earlier dynamo epoch, a weak late dynamo, and spontaneous remanence formed in a near-zero field. To further understand the source of the magnetization in young lunar samples, we conducted paleomagnetic, petrographic, and $^{40}Ar/^{39}Ar$ geochronometry analyses on a young impact melt glass rind from the exterior of ~3.35 Ga mare basalt 12017. Cosmic ray track densities and our $^{40}Ar/^{39}Ar$ and cosmogenic ^{38}Ar analyses constrain the glass formation age to be <7 Ma and most likely <20 thousand years (kyr), making it likely the youngest extraterrestrial sample yet studied with paleomagnetic methods. Despite its relatively high fidelity magnetic recording properties compared to most lunar rocks, we find that the glass carries no stable primary natural remanent magnetization and that it formed in a field <~7 μT (with a 2σ upper limit of <11 μT). Given the poor magnetic recording properties of the majority of lunar samples, this provides further evidence that many or perhaps even all previous paleointensity estimates for ≤1.5 Ga rocks are upper limits on the true paleofield and therefore require neither a protracted strong (>10 μT) core dynamo field nor impact-generated fields.

1. Introduction

Recent paleomagnetic studies of Apollo samples have demonstrated that the Moon had a core dynamo magnetic field of intensity ~20–110 μT between at least 4.25 and 3.56 billion years (Ga) [*Cournède et al.*, 2012; *Garrick-Bethell et al.*, 2009; *Shea et al.*, 2012; *Suavet et al.*, 2013; *Weiss and Tikoo*, 2014]. The dynamo field apparently declined precipitously to <4 μT by 3.19 Ga [*Tikoo et al.*, 2014]; it is currently unclear whether this inferred drop in paleointensity reflects a permanent decline (or cessation) of the lunar dynamo or a transient decrease in field intensity (i.e., resulting from magnetic field reversals or start-stop dynamo generation [*Scheinberg et al.*, 2015]). The low-fidelity magnetic recording properties [*Lawrence et al.*, 2008; *Tikoo et al.*, 2012] and poorly constrained thermal and deformational histories of the majority of young (<3.56 Ga) lunar rocks have thus far hindered paleomagnetic efforts to determine when the dynamo actually ceased [*Weiss and Tikoo*, 2014]. Most lunar thermal evolution models predict that a core dynamo powered solely by thermal convection could only persist to sometime between ~2.5 and 4.1 Ga [*Evans et al.*, 2014; *Laneuville et al.*, 2013; *Zhang et al.*, 2013] with the precise time depending sensitively on the critical heat flux for core convection and the amount of water in the lunar interior. A mechanical lunar dynamo driven by impact-induced rotational changes of the mantle could only generate fields until the end of the basin-forming impacts (~3.7 Ga) [*Le Bars et al.*, 2011]. On the other hand, a mechanical dynamo generated by mantle precession might last until as late as ~3.55–0.6 Ga depending on the poorly constrained lunar orbital evolution [*Dwyer et al.*, 2011; *Tian et al.*, 2014; *Tikoo et al.*, 2014]. Thus far, only lunar evolution models that consider thermochemical convection powered by core crystallization have found that the dynamo might persist beyond 0.6 Ga in either a continuous or start-stop regime [*Laneuville et al.*, 2014; *Scheinberg et al.*, 2015].

A key impediment to distinguishing between these hypothesized dynamo mechanisms is that there are presently no published modern paleointensity studies of lunar rocks with well-defined ages younger than 3.19 Ga. Nevertheless, an intriguing observation made by Apollo era (i.e., 1969 to early 1980s) lunar paleomagnetic studies is that rocks as young as ~2–200 million years old (Ma) appear to carry substantial remanent
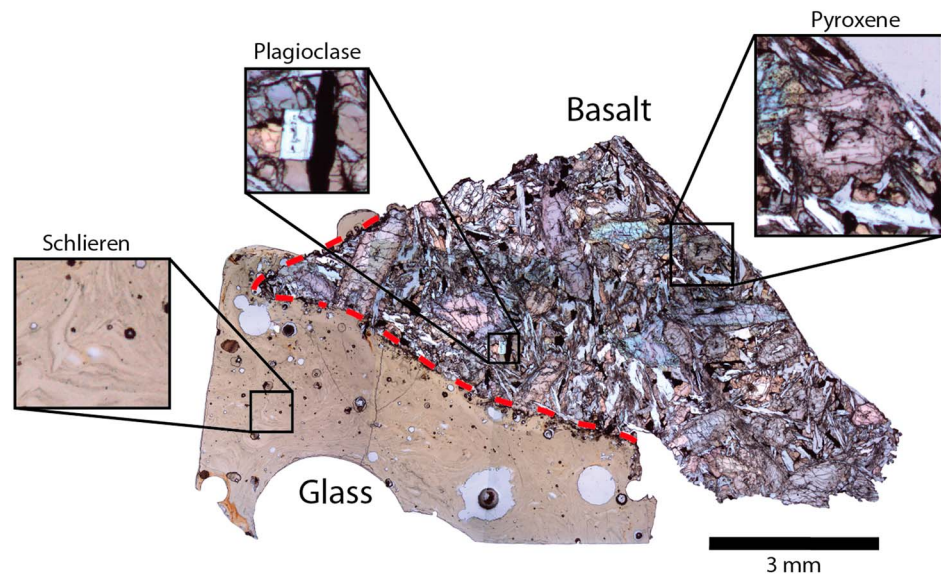
Figure 1. Transmitted plane-polarized light photomicrograph of a 30 µm thin section of Apollo sample 12017 (subsample, 63). The thin section transects the boundary from the basalt at the upper right to the vesicular glass rind at the lower left (boundary shown by red dashed line). We measured the pyroxene density and plagioclase [010] crystal widths (middle inset) to determine the cooling rate of the basalt (Figure S5). The augite rims (thick pink band surrounding darker core in right inset) surrounding the pigeonite are distinctive of the pigeonite basalt suite of lunar samples. The schlieren, apparent as dark bands in the glass (left inset), indicates an impact melt origin for the glass rind.

magnetization [see *Wieczorek et al.*, 2006, Figure 3.22]. If it is assumed that this magnetization is thermoremanent in origin, paleointensity estimates suggest that these rocks were magnetized in fields of ~1–20 µT [*Cisowski et al.*, 1983, 1976, 1977; *Dunn and Fuller*, 1972; *Gose et al.*, 1973; *Sugiura and Strangway*, 1980; *Sugiura et al.*, 1979]. However, there are many uncertainties associated with these young Apollo era measurements. Most importantly, because all of the previously analyzed samples are petrologically heterogeneous, impact-modified lithologies [*Fuller and Cisowski*, 1987], the origin and ages of their magnetization and the associated paleointensities of their magnetizing fields are extremely uncertain, even by the standards of lunar paleomagnetism. Alternatively, if we consider the Apollo era paleointensities to be accurate, a challenge arises in identifying the origin of the magnetizing fields.

Although core crystallization could account for a global dynamo field after ~0.6 Ga, it would be surprising if the dynamo persisted until just a few million years ago because this would appear to suggest that we are presently in a special observation window just after the dynamo vanished. There are at least three possible alternatives for how this young magnetization could have arisen. The first scenario is that the rocks were magnetized by fields transiently generated by recent meteoroid impacts. In particular, plasmas generated by the small-scale impacts expected after 3.7 Ga have been theoretically proposed to be capable of producing fields possibly reaching several milliteslas and lasting for ~1 s or less [*Crawford and Schultz*, 1999; *Schultz and Spudis*, 1983; *Srnka et al.*, 1979; *Tikoo et al.*, 2014]. Such a transient field could be recorded as a thermoremanent magnetization (TRM) by a sample cooling more rapidly than this timescale or as a shock remanent magnetization (SRM) by a sample subjected to high pressures [*Gattacceca et al.*, 2010]. However, evidence for impact-generated fields has yet to be identified even in terrestrial impact craters [*Carporzen and Gilder*, 2006; *Carporzen et al.*, 2012; *Louzada et al.*, 2008; *Weiss et al.*, 2010] and the physical processes by which they might be generated are highly uncertain. A second alternative is that young lunar rocks were magnetized by remanent crustal fields emanating from nearby magnetized rocks. However, the measured crustal fields at the Apollo sites appear to be too weak (ranging from ~330 to <6 nT) to account for the reported paleointensities [*Dyal et al.*, 1974]. Finally, given that the majority of young samples were analyzed using alternating field (AF) demagnetization, the inferred magnetizations may simply be artifacts due to acquisition of spurious laboratory anhysteretic remanent magnetization (ARM) or gyroremanent magnetization (GRM) during the demagnetization experiments [*Tikoo et al.*, 2012]. Related to this, it is also possible that the apparent natural remanent magnetization (NRM) in rocks containing a small number of large metal grains

is actually spontaneous remanence formed in a near-zero field. In the latter two cases, the inferred paleointensities would simply be upper limits and therefore would provide no evidence at all for a paleofield.

To resolve these ambiguities, we conducted paleomagnetic, petrographic, and $^{40}Ar/^{39}Ar$ chronometry analyses on a very young lunar impact glass from Apollo 12 sample 12017. We selected this sample because it is both petrographically simple compared with many other impactites (which are commonly multigeneration breccias) and is, within measurement uncertainties, the youngest lunar sample yet analyzed with paleomagnetic studies. Its extremely young age makes it very unlikely to have recorded a lunar dynamo, making it an ideal sample for distinguishing between the impact fields, crustal remanence, and zero-field magnetization hypotheses.

An overview of the NRM demagnetization data for this sample was presented in a previous study on the magnetic fidelity of lunar samples [*Tikoo et al.*, 2012]. The present work greatly expands the analysis of the demagnetization data, provides new petrologic data, and reports the first robust age and thermal history constraints on both the basalt and glass portions of the sample using $^{40}Ar/^{39}Ar$ thermochronometry, cosmic ray and surface exposure ages. Additionally, we provide a complete interpretation of the glass NRM components and develop a quantitative numerical model for the remanent field of the underlying basalt. This allows us to understand in detail the possible origin of any magnetization in the glass.

2. Sample Description

2.1. Sampling, Petrography, and Age

The focus of this study is a ~0.05–5 mm thick glassy rind overlying one of the exterior faces of the ~3.3 Ga quartz-normative, porphyritic, pigeonite basalt 12017 (Figures 1 and S3 in the supporting information) [*Horn et al.*, 1975; *Horz and Hartung*, 1971; *Warner*, 1970]. Sample 12017 was collected during the Apollo 12 mission, which landed in Oceanus Procellarum. Although not identified in photographs from the lunar surface, 12017 is thought to have been retrieved from a small glass-coated mound (Figure S4) because it is the only sample with a glassy exterior mentioned in the Apollo 12 astronaut transcripts.

The glass rind on 12017 consists of a homogeneous shiny black layer containing 0.1 to 3 mm diameter vesicles overlain by a minor quantity of second-generation darker glassy ellipsoids <1 mm to 2 mm in diameter [*Horz and Hartung*, 1971; *Warner*, 1970]. The glass contains some entrained crystals associated with schlieren, indicating that it is an impact melt (see Figure 1). No shock features such as microfracturing of plagioclase or the development of multiple twin lamellae in clinopyroxene are present in the interior of the basalt portion of 12017, indicating that it experienced maximum shock pressures of <5 GPa [*Sclar*, 1971]. Likewise, the lack of fracturing in the glass demonstrates that it too has been essentially unshocked since its formation. These textural observations, along with elemental compositional differences between the glass and basalt, indicate that the glass was splashed onto the basalt from a nearby impact rather than being formed by in situ shock melting of the underlying basalt [*Morgan et al.*, 1971]. This glass may have formed during the small impact that created the mound on which 12017 was discovered [*Warner*, 1970].

The glass apparently formed very recently. The bottom and top surfaces of the basalt have surface exposure (e.g., cosmic ray track) ages of 1.0 and 0.7 million years (Ma), respectively [*Fleischer et al.*, 1971]. These ages suggest that the basalt was likely flipped over into its present configuration at 0.7 Ma. The density of micrometeorite craters on the exterior surface of the glass, which overlies the top surface of the basalt, indicates a surface exposure age between 4 and 20 thousand years (kyr) [*Morrison et al.*, 1972], consistent with a 9 kyr surface exposure age inferred from cosmic ray track densities in the glass [*Fleischer et al.*, 1971]. This age is also consistent with our measured ^{38}Ar cosmic ray exposure age for the glass of 0.017 ± 0.023 Ma (see section 4).

The 4–20 kyr surface ages should set a minimum age for the formation of the glass. In fact, we propose that they likely represent the formation age itself. This is because the glass, being splatter from a nearby impact, must have been emplaced while the rock was on the surface. If the exposure age is not an igneous formation age and instead reflects relic exposure from an earlier period of surface residence, then the glass would be required to have been exposed at the surface for at least two separate episodes lasting for a cumulative time of 4–20 kyr and buried or at least flipped over and then exhumed again in between these episodes. This is highly unlikely because for >90% of the rocks with the size of 12017, such a turnover event only occurs every
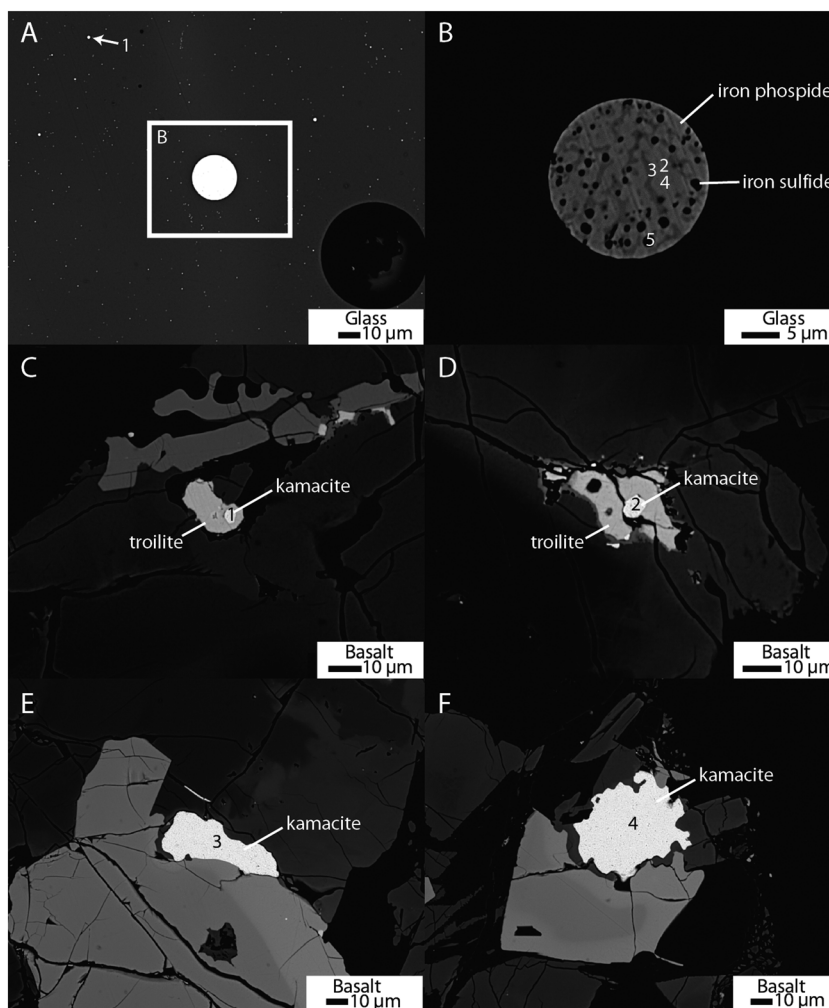
Figure 2. Backscattered scanning electron microscope images of thin section 12017,63 showing habit and textures of metal grains (bright phases) and surrounding silicate minerals (darker phases). Numbers in each correspond to microprobe compositional measurements identified in Table S2.

few million years [*Horz et al.*, 1975], longer than the cumulative surface exposure time of the basalt. Therefore, it is likely that the rock was excavated to the surface for the first time at 1.7 Ma (as given by the sum of exposure ages of the bottom and top of the basalt), flipped over at 0.7 Ma, and then splashed with glass at 4–20 kyr ago [*Fleischer et al.*, 1971]. As shown later, this chronology is consistent with our measured <7 Ma ^{40}Ar/^{39}Ar age of the glass. The extraordinarily young age of the glass portion of the sample makes it a fascinating and unique target for investigating the source of magnetization formed during recent lunar history.

2.2. Ferromagnetic Mineralogy

We used rock magnetic and electron microscopy measurements to determine the identity and mean crystal size of the ferromagnetic minerals in the glass and basalt. Our backscattered electron microscopy and wavelength dispersive spectroscopy (Figure 2 and Table S2) indicate that the primary ferromagnetic minerals in the basalt portion of 12017 are ~3–5 µm diameter kamacite (α-Fe) grains associated with troilite and ~50 µm diameter isolated nearly pure Fe kamacite grains with composition $Fe_{0.99-1}Ni_{0-0.01}$ [*Tikoo et al.*, 2012]. The glass rind contains ≤1 µm diameter grains of nearly pure Fe kamacite and ~20 µm diameter grains of iron phosphide with inclusions of ≤1 µm diameter iron sulfide [see *Tikoo et al.*, 2012, supplementary section 2.2]. Our hysteresis loops indicate that both lithologies are dominated by grains in the multidomain size range (see supporting information section 1.1 in Text S1) [*Tikoo et al.*, 2012].

2.3. Cooling Rate Determination and Implications for NRM

As discussed previously [*Garrick-Bethell et al.*, 2009; *Shea et al.*, 2012; *Suavet et al.*, 2013], important evidence constraining the origin of NRM in lunar rocks is provided by their cooling rates. In particular, for samples with an NRM, a cooling timescale from the 780°C kamacite Curie point to ambient surface temperatures exceeding 1 day indicates that the magnetizing field was stable and long lived like that expected from a core dynamo or crustal magnetization rather than putative transient meteoroid impact-generated plasma fields. To estimate the cooling rate of the basalt, we measured widths of the [010] face of plagioclase laths and the areal number density of pyroxene crystals following *Grove and Walker* [1977] (Figure S5). Our measurements indicate a cooling rate of ~0.35°C/h at 1120°C, yielding a minimum cooling time of ~2.5 months from the kamacite Curie point (780°C) to the maximum daily surface temperature on the Moon (~120°C), assuming a constant cooling rate. There have been no cooling rate studies of the glass rind. However, given the rind thickness of $l = 0.05–5$ mm and a typical silicate rock thermal diffusivity of $D \sim 10^{-6}$ m^2 s^{-1}, we estimate the time for cooling from the kamacite Curie point after deposition on the cold basalt [see *Carslaw and Jaeger*, 1959], $\tau \sim l^2/D \sim 0.03–30$ s (i.e., longer than any likely impact generated field at this time).

3. NRM Behavior

3.1. Introduction and Methods

We studied the magnetization of mutually oriented subsamples from both the glass and basalt portions of 12017. All of our subsamples originated from the exterior surface of two large pieces (12017,3 and 12017,4) cut from the main mass of 12017 at NASA Johnson Space Center (JSC) with a wire saw in 1970 (Figures S3a and S3b). In particular, our individual subsamples were prepared from three parent composite basalt-glass JSC subsamples: 12017,12 and 12017,13 (both from slab 12017,4), and 12017,59 (from slab 12017,3) (Figure S3b). Samples 12A, 12B, 13A, and 13B were all separated in 1970 at JSC, while we produced additional subsamples using a wire saw and chipping at Massachusetts Institute of Technology (MIT) ~40 years later.

The mutual orientations of our subsamples were reconstructed from sketches and photographs of initial sample processing at JSC in 1970 (Figure S3). To facilitate accurate sample orientation during subsampling at MIT, this study employs a new orientation system that is rotated counterclockwise by 16° along the east axis relative to that used in the original saw cut diagrams (Figure S3c). After the arrival of the samples at MIT, nearly all sample preparation and NRM measurements were performed in a class 10,000 clean, magnetically shielded room (ambient magnetic field strength ~200 nT) in the MIT Paleomagnetism Laboratory. The magnetometer used in this study has a sensitivity of approximately ~10^{-12} Am^2 and blank holder measurements are typically ~$1–8 \times 10^{-12}$ Am^2 before vector subtraction.

Tikoo et al. [2014] recently showed that Apollo era cutting using a circular saw at JSC sometimes significantly contaminated the remanent magnetization of lunar samples with a weak NRM by leaving a residue of metal and/or heating the surface while in Earth's magnetic field. Although sample processing of 12017 used a wire saw and not a circular saw, we sought to mitigate any potential metal surface contamination by sanding the JSC saw cut faces of the four samples drawn from parent samples 12 and 13 (labeled 12A, 12B, 13A, and 13B) using silica carbide sandpaper in a magnetically shielded room. Parent sample 59 was not sanded because of its fragility. We measured the NRM of the four samples repeatedly throughout the course of sanding. As a control, we also sanded acid-washed, weakly magnetized, 2.5 cm diameter round Ge 124 quartz disks and found that the sanding process did not introduce any magnetization onto the disks ($<5 \times 10^{-12}$ Am^2 per disk).

Following sanding, we further subdivided parent samples 12A, 13A, and 13B to obtain 10 final subsamples for the demagnetization experiments, each individually composed of either pure basalt or pure glassy rind (Figure S3c and Table S3). Seven of these subsamples were selected for in-depth study and demagnetization analyses. All seven subsamples were subjected to static three-axis alternating field (AF) demagnetization up to at least 85 mT, with some subsamples further demagnetized to 290 mT. For each AF level, we first applied an AF in the three orthogonal directions to demagnetize the sample. Then AFs at the same field level were again applied along each axis individually, with the NRM measured after the AF application along each axis. This process was repeated between 2 and 4 times. The final magnetic moment for each AF step was
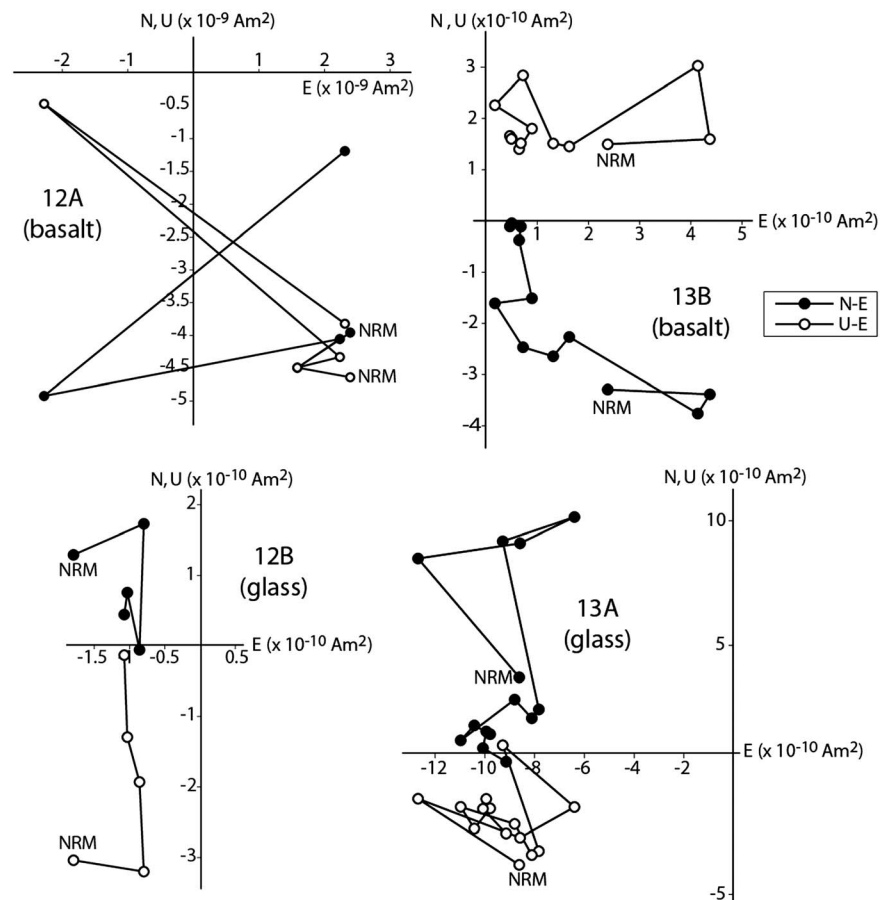
Figure 3. The effect of sanding on the NRM of 12017. Shown is a two-dimensional projection of the NRM vectors of basalt subsamples 12A and 13B and glass samples 12B and 13A during progressive sanding stages. Solid symbols represent the end points of the magnetization vector projected onto the horizontal north-east (N-E) planes, and open symbols represent projections onto the vertical up-east (U-E) planes. Points labeled "NRM" represent the magnetization prior to sanding, while subsequent points show the evolution of the magnetization during progressive sanding steps.

calculated as an average of the moments measured after each single-axis demagnetization following the Zijderveld-Dunlop protocol, which mitigates the effects of spurious GRM and ARM acquisition [*Stephenson*, 1993]. All paleomagnetic measurements were acquired using a 2G Enterprises Superconducting Rock Magnetometer with automated sample handling and demagnetization equipment [*Kirschvink et al.*, 2008] in the MIT Paleomagnetism Laboratory.

We used principal component analysis (PCA) to determine the best fit directions of any observed magnetization components [*Kirschvink*, 1980]. We then compared the deviation angle (DANG) and maximum angular deviation (MAD) values [*Tauxe and Staudigel*, 2004] to qualitatively assess whether each component trended toward the origin. In this test, the angle between the component direction and a line connecting the origin to the centroid of the data (DANG) is compared with the MAD of the component. If the MAD is greater than the DANG, the component appears to be origin trending.

3.2. Previous Work on 12017

Prior to the analyses by *Tikoo et al.* [2012], the only previous AF demagnetization study of 12017 was conducted by *Strangway et al.* [1971], who analyzed two mutually oriented 12017 basalt subsamples. The latter study tentatively identified two NRM components: a low-coercivity (LC) magnetization blocked up to a peak AF field of 5 mT and a higher-coercivity (HC) magnetization blocked from 5 to 20 mT, respectively. After AF demagnetization to 20 mT, the magnetization directions of the two subsamples were roughly similar in orientation (~30° apart).
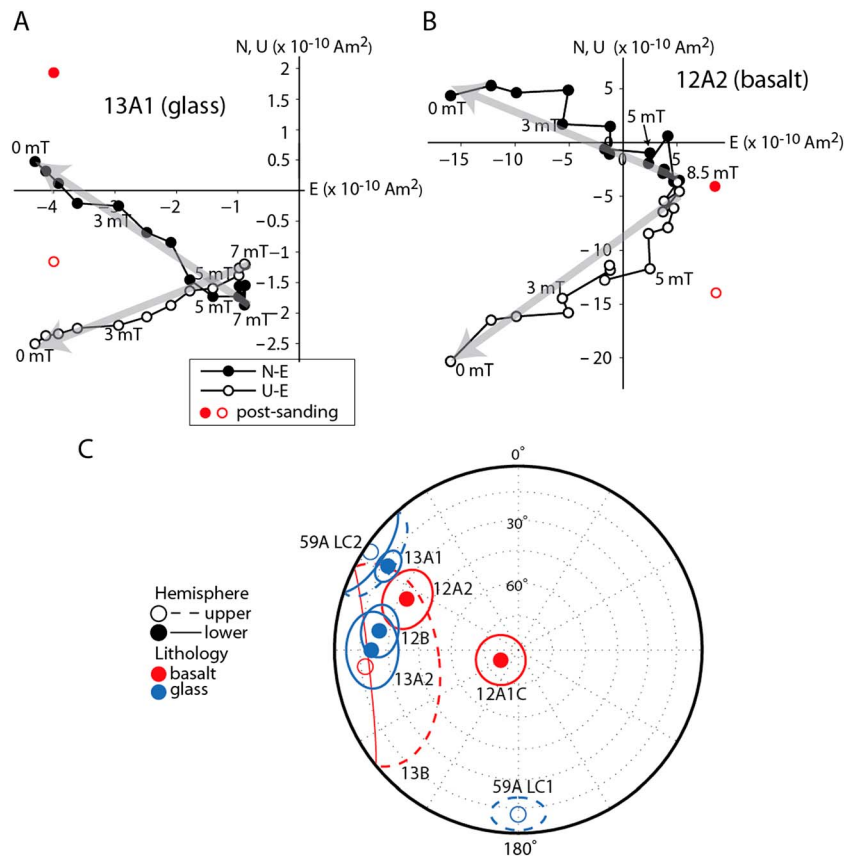
Figure 4. AF demagnetization over the coercivity range of the LC component for selected 12017 samples. The magnetization step labeled "postsanding" was measured after sanding but prior to further subdivision and scaled in intensity to the mass of the subsample relative to its parent sample, while the "0 mT" step was measured following subdivision but prior to beginning AF demagnetization. (a, b) Two-dimensional projection of the endpoints of the magnetization vectors during AF demagnetization. Solid symbols represent projection onto the horizontal N-E planes, and open symbols represent projections onto the vertical U-E planes. Peak fields for selected AF steps are labeled in milliteslas. The LC component is labeled with grey arrows. (c) Equal area stereographic projection of LC components obtained from PCA fits and their associated MAD ellipses. Open symbols and dashed lines represent the upper hemisphere, and solid symbols and solid lines represent the lower hemisphere. LC demagnetization data for all other subsamples are shown in Figure S6.

3.3. Sanding

The total mass lost from each 12017 sample during sanding at MIT ranged between 1 and 9% of the original sample mass (Table S4). Despite removing such small amounts of material, sanding resulted in dramatic changes in the magnetic moments of some samples (Figure 3): the moment intensities changed between 13% and 60% and the moment directions experienced large angular changes. The magnetization changes were nonlinear and noisy (PCA fits to the demagnetization trends had MAD values up to 27°). The magnetization directions of the subsamples were collectively scattered both before and after sanding.

3.4. LC Magnetization

As previously mentioned, some samples were further subdivided following sanding. The magnetization directions of each of the subdivided samples sometimes were substantially different from the measurements of their predivided parent samples, indicating that the parent samples were nonunidirectionally magnetized (Figure 4). AF demagnetization of all sanded subsamples revealed a LC component blocked up to ~10 mT (Figures 4a, 4b, and S6). The LC magnetization was largely unidirectional across subsamples from parent JSC block 12017,4 (i.e., all subsamples except for 59) (Figure 4c). Glass sample 59A displayed two apparent LC magnetization components that we label LC1 and LC2, with the latter oriented like the LC components
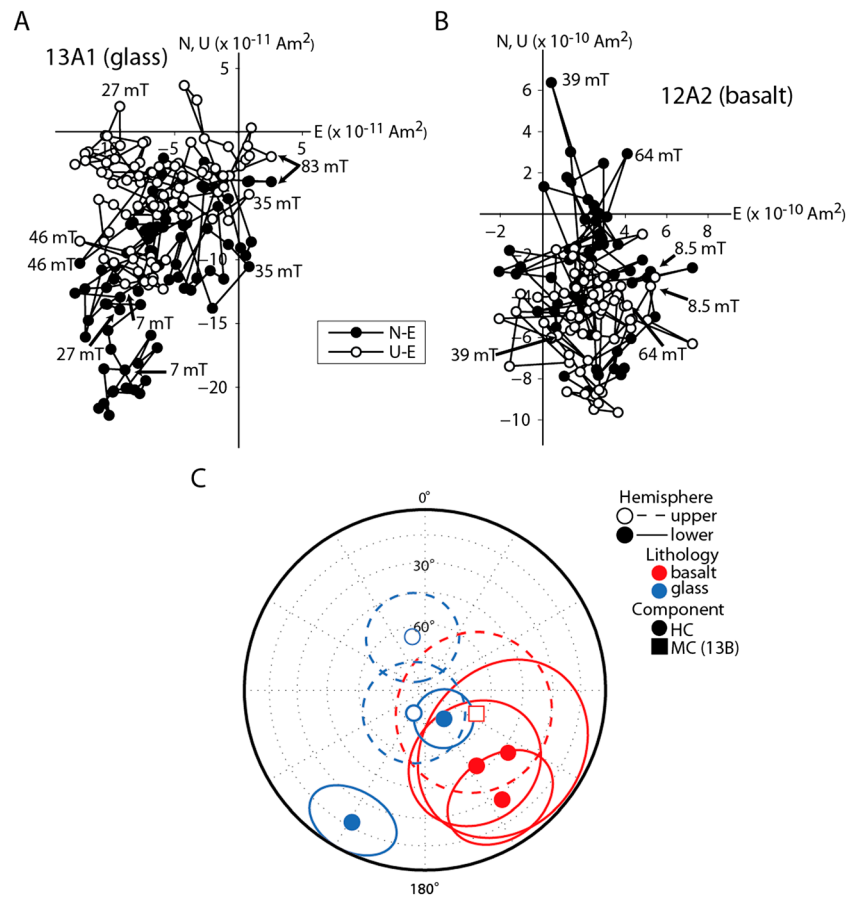
Figure 5. Demagnetization of 12017 over the HC coercivity range. (a, b) Two-dimensional projection of the NRM vectors during AF demagnetization. Solid symbols represent the end points of the magnetization vector projected onto the horizontal N-E planes, and open symbols represent projection onto the vertical U-E planes. Selected AF field steps are labeled in milliteslas. HC demagnetization data for all other subsamples are shown in Figure S8. (c) Equal area stereographic projection of PCA fits to the MC and HC magnetization. Symbols represent fit directions, and surrounding ellipses represent associated MAD values. Open symbols and dashed lines represent the upper hemisphere, and solid symbols and solid lines represent the lower hemisphere.

of the other samples (Figures 4c and S6). DANG/MAD tests indicate that the LC components in all samples are not origin trending and are therefore unlikely to represent primary magnetization.

3.5. NRM Behavior at Higher Coercivities

We observed no unambiguous higher-coercivity NRM components (i.e., magnetization blocked above ~10 mT) in either the basalt or glass portions of 12017 (Figures 5a, 5b, and S8). Despite the absence of stable NRM at high AF levels, *Tikoo et al.* [2012] tentatively fit HC magnetization components to the 12017 demagnetization data from the end of the LC component up to a maximum of ~85 mT. Additionally, a potential medium-coercivity (MC) component for sample 13B1 can be fit from 12 to 54 mT, although the fit direction does not lie near any of the other fit components and does not pass the DANG/MAD test (Figure 5c). The HC magnetization fits for the glass subsamples were nonunidirectional (Figure 5c). The fit HC magnetization directions for the basalt subsamples, on the other hand, are somewhat clustered (within ~90° of one another) (Figure 5c), broadly consistent with the prior observations by *Strangway et al.* [1971]. However, none of the MC or HC fits assigned by *Tikoo et al.* [2012] for either the basalt or glass lithologies are origin trending according to the DANG/MAD test [*Tikoo et al.*, 2012] and, as described in section 5.1 below, most of the HC paleointensities are within error of zero. Additionally, the large scatter in the NRM demagnetization data at high AF levels suggests that the samples are demagnetized, with any remaining magnetization potentially a result of spurious ARM. Therefore, the apparent clustering of the HC fit directions for the basalt hints at, but does not provide robust evidence for, an underlying NRM component blocked in the HC range.
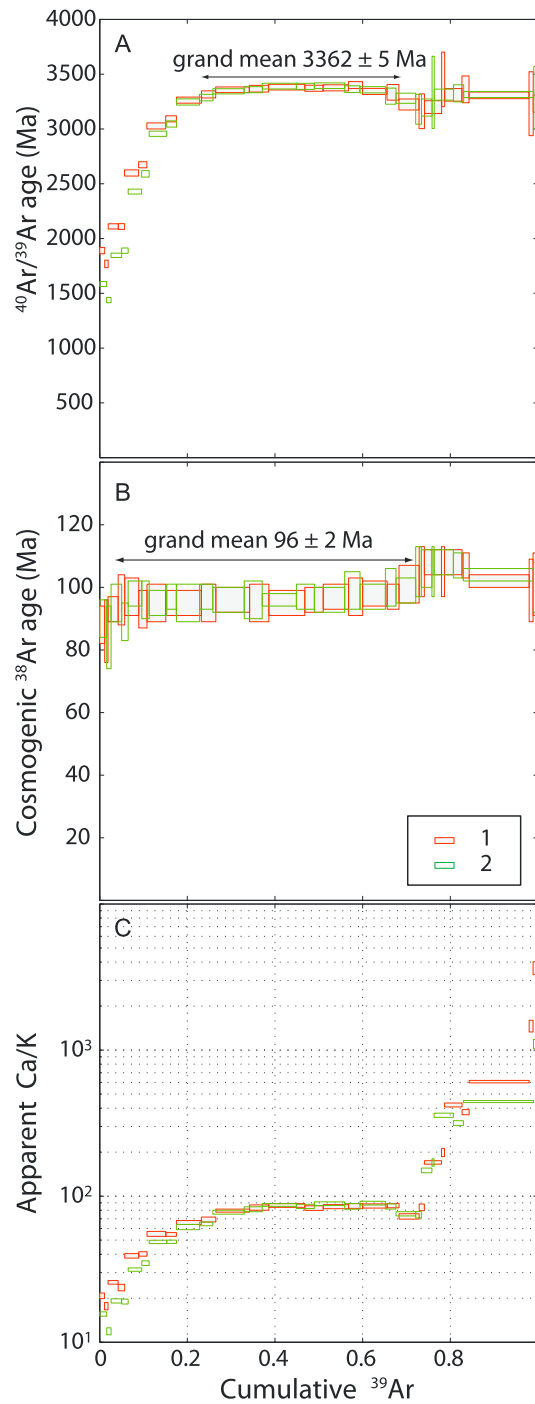
Figure 6. Ar isotopic analyses of the 12017 basalt sample 12A. (a, b) Apparent $^{40}Ar/^{39}Ar$ age and cosmogenic ^{38}Ar exposure age release spectra for two basalt aliquots (1 and 2). Each spectrum is plotted against the cumulative release fraction of ^{39}Ar. The ^{38}Ar release spectrum is calculated following *Shuster and Cassata* [2015]. Dimensions of boxes indicate $\pm 1\sigma$ (vertical) and the fraction of ^{39}Ar released (horizontal). Error-weighted mean plateau ages and uncertainties are labeled. (c) Corresponding apparent Ca/K ratios.

4. $^{40}Ar/^{39}Ar$ and Cosmogenic ^{38}Ar Geochronology

To use the 12017 glass as a constraint on lunar paleointensities, we need to determine its formation age. Unfortunately, lunar impact glass is difficult to date using the $^{40}Ar/^{39}Ar$ method due to large amount of trapped (i.e., nonradiogenic) ^{40}Ar and solar wind ^{36}Ar [e.g., *Husain*, 1974]. The only existing data constraining the formation time of the 12017 basalt appear in an abstract by *Horn et al.* [1975], who reported a $^{40}Ar/^{39}Ar$ plateau age for the basaltic portion of 12017 of 3.19 ± 0.07 Ga with few measurement details. To constrain the timing of glass formation, our strategy was to (i) determine the glass crystallization age and (ii) assess evidence for any late-stage reheating of the 12017 mare basalt host resulting from the glass splash event as recorded by $^{40}Ar/^{39}Ar$ thermochronology applied to the basalt. Furthermore, we (iii) used the ^{38}Ar exposure age of the host rock to place a conservative upper bound on the glass-forming impact event under the assumption that the impact glass formed at the lunar surface. We then (iv) applied $^{40}Ar/^{39}Ar$ geochronology directly to the impact glass to place a less restrictive (i.e., due to the possibility of trapped Ar components), but nevertheless important constraint on the glass formation timing. Analytical details of the $^{40}Ar/^{39}Ar$ and cosmogenic ^{38}Ar measurements can be found in Text S2.

Analyses of two basalt aliquots produce remarkably similar $^{40}Ar/^{39}Ar$ release spectra (Figure 6a). We calculated error-weighted $^{40}Ar/^{39}Ar$ plateau ages of 3347.1 ± 5.1 Ma and 3343.7 ± 4.9 Ma from each aliquot, with a mean age of 3345 ± 5 Ma between the aliquots (uncertainties here and below are 1σ; uncertainty in the decay constant and age of the fluence monitor are excluded). The release spectra also both show evidence of late-stage open system behavior in the K/Ar system, with initial step ages of 1572 ± 11 Ma and 1876 ± 14 Ma for each aliquot. If the discordance in $^{40}Ar/^{39}Ar$ step ages resulted from diffusive loss of ^{40}Ar at elevated temperature due to the glass splash event, these data require that the glass splash event occurred at, or more recently than, ~1570 Ma [*Shuster et al.*, 2010]. The cosmogenic ^{38}Ar release spectra for the two aliquots are also similar (Figure 6b), with a mean apparent exposure age of 96.3 ± 1.5 Ma. Assuming
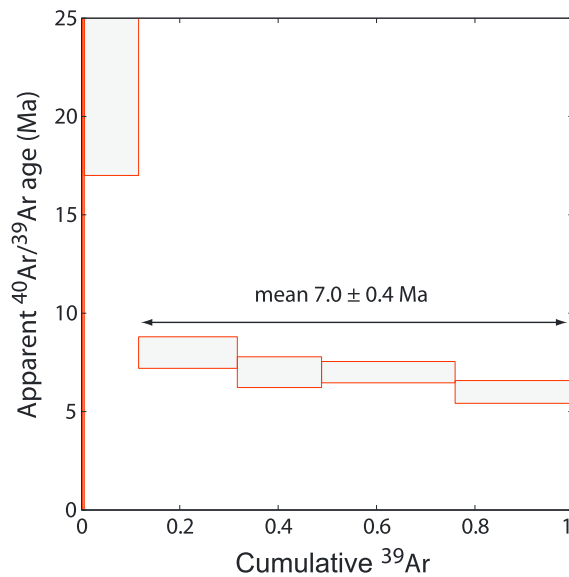
Figure 7. Apparent ^{40}Ar/^{39}Ar age release spectrum for 12017 glass sample 13B2. The spectrum is plotted against the cumulative release fraction of ^{39}Ar. Dimensions of boxes indicate ±1 standard deviation (vertical) and the fraction of ^{39}Ar released (horizontal). Error-weighted mean plateau age and uncertainty are labeled.

the glass-forming event occurred during or after the sample was delivered to the surface, the glass would then be required to be $\leq$ ~96 Ma.

Finally, the ^{40}Ar/^{39}Ar release spectra of the 12017 impact glass are complex, with most extractions below the detection limit (indicative of low abundances of K and radiogenic ^{40}Ar) and evidence of parentless ^{40}Ar released at the initial extractions (i.e., sequentially decreasing ^{40}Ar/^{39}Ar step ages with cumulative ^{39}Ar; Figure 7 and Table S1). Despite these complexities, concordant step ages observed at the four highest temperature extractions provide an error-weighted mean of 7.0 ± 0.4 Ma. Because they were observed at high extraction temperatures (between 560 and 1325°C), these data most likely reflect gas derived from mineral inclusions (which have low Ar diffusivity) held within the impact glass. For this reason, and due to the possibility of nonradiogenic ^{40}Ar, we consider the apparent plateau age to provide a crude upper bound of the glass formation timing. Taken together, the basalt and glass ^{40}Ar/^{39}Ar and ^{38}Ar data indicate that the glass most likely formed $\leq$ ~7 Ma. Although poorly determined, our measured cosmogenic ^{38}Ar exposure age for the glass (0.017 ± 0.023 Ma; Table S1) corroborates this finding. This is consistent with, although less restrictive than, the <20 kyr age inferred from surface exposure ages (section 2.1).

5. Paleointensity

5.1. Paleointensity Estimations

We employed the ARM and isothermal remanent magnetization (IRM) normalization methods to estimate the paleointensity of the fields in which the 12017 basalt and glass formed. Using the assumption that the NRM components have a thermally activated origin [e.g., TRM, partial TRM (pTRM), or viscous remanent magnetization (VRM)], the paleointensities may be calculated using the following formulas:

$$\text{ARM paleointensity in } \mu T = (NRM/ARM) \cdot (\text{dc bias field}) / f' \qquad (1)$$

$$\text{IRM paleointensity in } \mu T = (NRM/IRM) \cdot a \qquad (2)$$

where f' is the TRM/ARM ratio and a is a calibration constant with units of μT that is inversely proportional to the TRM/IRM ratio [*Garrick-Bethell et al.*, 2009; *Shea et al.*, 2012; *Suavet et al.*, 2013].

As with previous applications of these methods, the majority of the uncertainty in the ARM and IRM paleointensity estimates originates from the poorly constrained calibration values of a and f', which vary due to grain size and shape. Here we adopt values of 1.34 for f' and 3000 μT for a [*Gattacceca and Rochette*, 2004; *Stephenson and Collinson*, 1974]. *Weiss and Tikoo* [2014] compiled a comprehensive list of calibration values from the literature and found that 95% (i.e., within lognormally distributed 2σ of the mean value) of multidomain FeNi-bearing samples have a values between 425 μT and 10060 μT and f' between 0.9 and 1.8 (see Table S2 of their supplementary online material). We utilize this wider range of f' and a values to quantify the range of possible paleointensities given the uncertainties in the calibration constant values. A second source of uncertainty is associated with the least squares regressions in the paleointensity plots of NRM lost versus ARM gained or IRM lost. We estimated these by computing 95% confidence intervals using a two-tailed Student's t test [*Weisberg*, 1985] on the linear paleointensity slopes. The purpose of the t test is to establish whether the associated paleointensity values are distinguishable from zero (i.e., to demonstrate that the ancient field was not null).
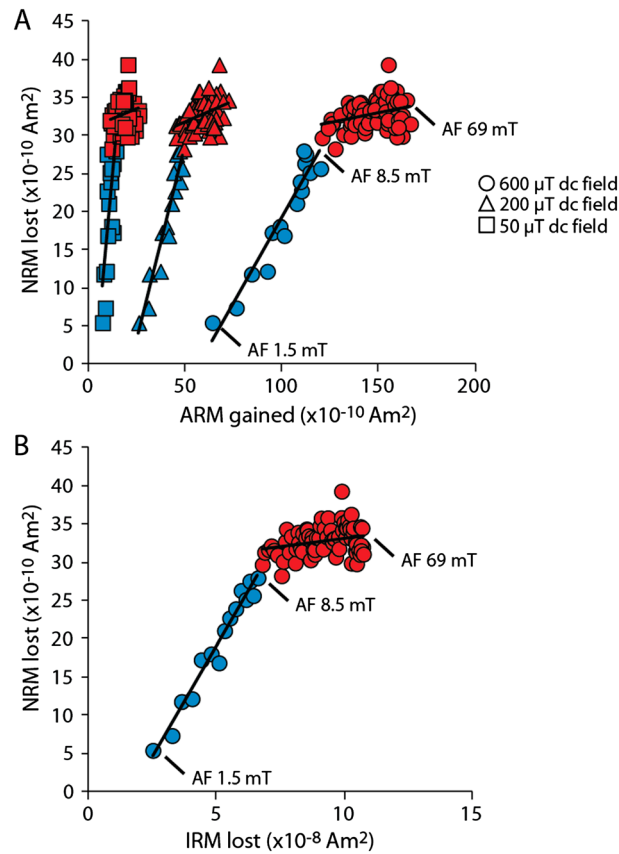
Figure 8. ARM and IRM paleointensity experiments for 12017 basalt sample 12A2. Shown is NRM lost during AF demagnetization as a function of (a) ARM gained during stepwise ARM acquisition and (b) IRM lost during stepwise AF demagnetization of a saturating IRM. Points corresponding to the LC components are shown in blue, and data from higher AF levels (HC) are shown in red.

Tikoo et al. [2012] reported NRM/ARM and NRM/IRM ratios for the LC magnetization observed in our 12017 subsamples. They also reported these ratios for their tentative HC fits and a separate specified range of AF levels for certain subsamples (typically 23–85 mT). Using $f' = 1.34$ and $a = 3000\,\mu T$, paleointensity values corresponding to the LC components of the basalt and glass portions range from 57 ± 23 to $223 \pm 35\,\mu T$ and from 22 ± 8 to $295 \pm 33.3\,\mu T$, respectively. Using the aforementioned 2σ, ranges of values for f' and a yield basalt LC paleointensities ranging from 42.7 ± 17.8 to $573 \pm 62\,\mu T$ and glass LC paleointensities ranging from 3.1 ± 1.1 through $991 \pm 1116\,\mu T$. Note that these values were obtained under the assumption that the relevant magnetization components have a thermal origin, which is unlikely (section 6.2). The linear regressions of NRM lost versus ARM gained and NRM lost versus IRM gained associated with these LC paleointensity estimates have uncertainties which are less than the fitted values, indicating that they are not consistent with a null paleofield (Table S5).

Paleointensity values corresponding to the HC range (i.e., the AF levels from the end of the LC component up to 85 mT) range from 4 ± 4 to 22 ± 13 and from 6 ± 2 to $18 \pm 5\,\mu T$ for the basalt and glass, respec-

tively (Figures 8 and 9). Similarly, using the wider range of calibration factors mentioned above, we get HC range paleointensities from 0.2 ± 4 to 198 ± 100 and 1 ± 0.1 to $43 \pm 13\,\mu T$ for the basalt and glass, respectively. For the basalt portion, the linear regressions associated with most HC paleointensity estimates have uncertainties indicating that the paleointensities are within error of zero or the recording capabilities of the rock (section 6.3 and Table S5). For the glass portion, half of the inferred paleointensities using $f' = 1.34$ (Table S5) are within error of the sample's ~7 μT paleointensity fidelity limit and are therefore also consistent with weak to null paleofields (section 5.2 and Table S5).

5.2. Paleointensity Fidelity Limit Tests

Samples with predominantly multidomain grains magnetized in the presence of weak to null magnetic fields are highly susceptible to the acquisition of spurious ARM during AF demagnetization [*Tikoo et al.*, 2012]. This is because, as the demagnetization experiment proceeds, the magnetic moment contribution from spurious ARM increases until the remaining NRM is obscured by noise at high AF levels. This ultimately means that a given sample has a minimum threshold paleointensity that can be accurately recovered using AF methods (which we refer to as the paleointensity fidelity limit). Here we seek to determine the maximum possible paleofield consistent with the observed lack of stable HC remanence in the basalt and glass portions of 12017.

Tikoo et al. [2012] previously reported paleointensity fidelity limits of ~15 and ~7 μT for the basalt (subsample 12A1C) and glass (subsample 13A2) lithologies of 12017, respectively. These estimates were obtained by imparting the samples with laboratory ARMs using an AC field of 85 mT and DC bias fields ranging from 3 to 200 μT (as an analog for TRM acquired in fields ranging from 2 to 150 μT). These laboratory ARMs were
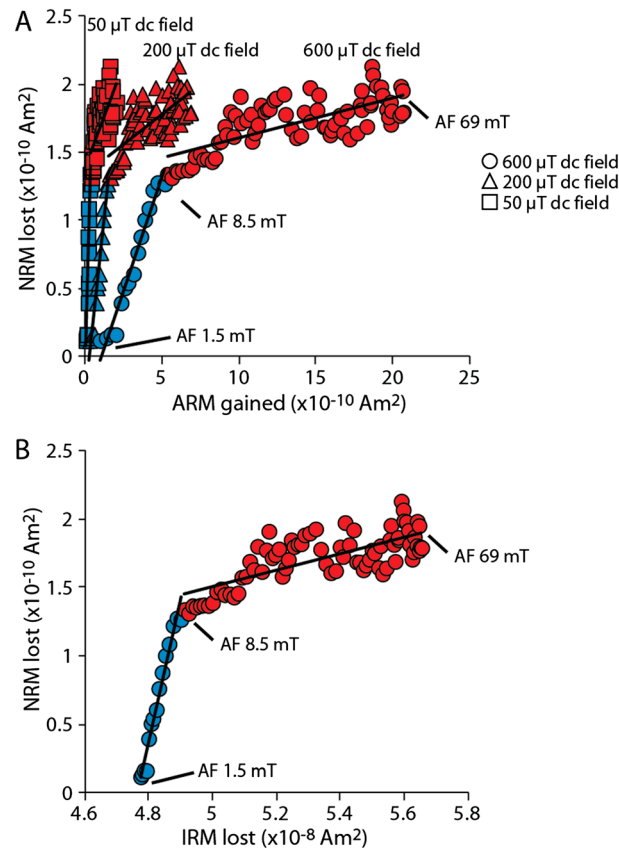
Figure 9. ARM and IRM paleointensity experiments for 12017 glass sample 12B. Shown is NRM lost during AF demagnetization as a function of (a) ARM gained during stepwise ARM acquisition and (b) IRM lost during stepwise AF demagnetization of a saturating IRM. Points corresponding to the LC components are shown in blue, and data from higher AF levels (HC) are shown in red.

subsequently AF demagnetized, and the ARM method was used to retrieve a paleointensity estimate over the coercivity range from 0 to 85 mT.

We computed new paleointensity limits using the revised method of *Tikoo et al.* [2014] which only includes AF levels above the end of the LC component. This new method is slightly more conservative because it estimates a fidelity limit for only the HC range rather than including lower coercivity ranges overprinted by recent remagnetization events. With this revision, we found that the glass portion of 12017 has a paleointensity fidelity limit of ~7 μT (subsample 12B) and the basalt has a limit of ~37 μT (subsample 12A1C), using a calibration constant f' of 1.34. Using a more conservative f' value of 0.9 (see above), the fidelity limits become ~55 μT for the basalt and ~11 μT for the glass. These paleointensity fidelity limits indicate that the strength of lunar surface fields at 3.3 Ga (the basalt formation age) and <7 Ma (the glass formation age) were likely <~37 μT and <~7 μT, respectively (or <~55 μT and <~11 μT using the extreme f' value). The basalt fidelity limits are broadly consistent with the more restrictive paleofield upper limit of ~4 μT at 3.19 Ga obtained from sample 12022 [*Tikoo et al.*, 2014].

The LC paleointensities (Table S5) exceed the above paleointensity limits, indicating that the LC magnetization is likely a true NRM component rather than spurious ARM, GRM, or spontaneous remanence from formation in a weak field. However, most of the apparent paleointensities (including uncertainties) for the HC magnetization range lie below or within error of the paleointensity fidelity limits (or even zero) for the two lithologies. Therefore, any paleointensities retrieved from the HC magnetizations in either the basalt or glass portions should be treated as upper limits on the field strength at the time when these lithologies last cooled to ambient temperatures.

6. Origin of the NRM

6.1. Sanding Components

As described in section 3.3, gentle sanding of 1970 JSC saw cut faces led to changes in the NRM intensity that greatly exceed the fraction of sample mass removed. We conclude that either these faces were locally remagnetized and/or contaminated by sample handling by the astronauts or at JSC, as has been documented for other Apollo 12 basalts by *Tikoo et al.* [2014]. Such contaminating magnetization is significant for 12017 because of the lack of a strong stable underlying lunar NRM (see below).

6.2. LC Components in Basalt and Glass

The approximately linear demagnetization trends of the LC magnetization suggest that it is a true NRM component rather than spurious remanence from the measurement process. This is consistent with the fact that the retrieved LC paleointensities are larger than the paleointensity fidelity limit in the LC range. Given that many of our subsamples (12A, 12B, 13A, 13B, and 59) were separated from one another more than 40 years
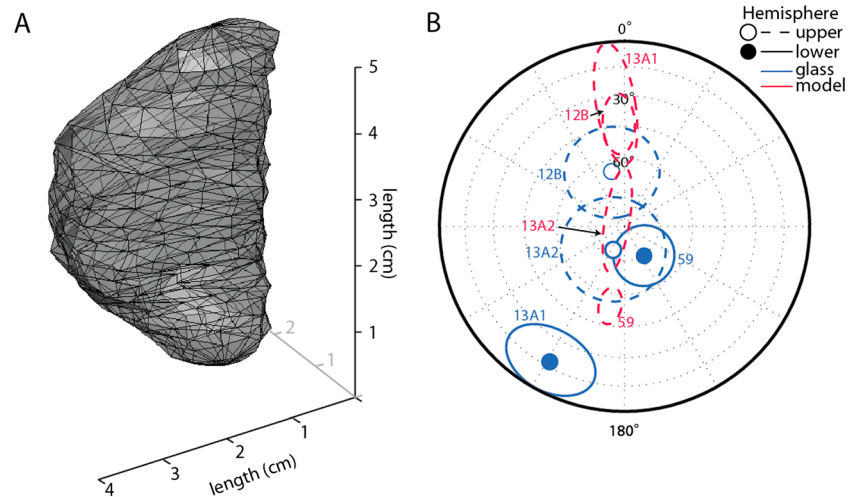
Figure 10. (a) Three-dimensional digital model of 12017 whole rock made from triangular facets. (b) Predicted remanent magnetic field from 12017 basalt at locations of glass subsamples (red) compared to magnetization directions fit to HC range of each subsample (blue). Shown are the computed magnetic field directions assuming a unidirectionally magnetized volumetric model with intensity equivalent to that expected for a total TRM acquired in a paleofield of 37 μT (upper limit on paleointensity recorded by basalt). Red ellipses denote estimated uncertainty of calculated field direction (see text), while subsample names are labeled next to each predicted field direction and measurement.

ago and have been in different orientations over the intervening period, the approximate unidirectionality of the LC component amongst all samples of both basalt and glass lithologies (including the LC2 component of 59A) demonstrates that it was likely acquired prior to subdivision at JSC in 1970. Therefore, we can exclude VRM acquired during exposure to the Earth's field as a possible explanation of the LC component. This conclusion is also supported by our laboratory VRM experiments (supporting information section 1.2 in Text S1), which suggest that VRM could only account for up to ~11% of the total measured NRM and for up to 35% of the LC components. We have also considered SRM as a potential source of the LC magnetization but find that it is easily removed at very low AF steps, unlike our LC magnetization (supporting information section 1.3 in Text S1). The high ratios of NRM to IRM over the LC coercivity range (ranging up to 10%) (Table S5) support the origin of the LC component as an IRM acquired during transport from the Moon in the presence of strong fields in the spacecraft [*Pearce et al.*, 1973] and/or sample handling at JSC from exposure to strongly magnetized materials. As expected for a low-field IRM, it is much less stable to AF demagnetization than a saturation IRM (Figure S7). Although the LC component also demagnetizes like a laboratory ARM, it is unlikely to be a pTRM or TRM from sawing because 12017 has only been cut with a wire saw (unlike the circular saw that has been found to have heated other Apollo samples [*Tikoo et al.*, 2012]). In any case, the low-peak coercivity and nonorigin trending nature of the LC component indicate that it is highly unlikely to be a full TRM acquired during primary cooling of either 12017 lithology on the Moon.

6.3. HC Magnetization

The HC magnetizations in the basalt and glass lithologies demagnetized erratically and are not origin trending. Furthermore, for most subsamples, the HC paleointensities are within error of zero and/or below the paleointensity fidelity limits of ~37 μT and ~7 μT for the two respective lithologies. The erratic demagnetization behavior of the NRM is emphasized by comparison with that of laboratory IRM and ARM (Figure S9). Therefore, we find no compelling evidence for primary NRM in the basalt or the glass of 12017.

7. Comparison With Remanent Fields at Apollo 12 Site and From 12017 Basalt

The observed absence of stable HC magnetization indicates that ambient fields were likely <7 μT (and almost certainly <11 μT) when the glass formed. This is broadly consistent with the very weak (~38 nT) ambient surface field measured at the Apollo 12 landing site. We show next that this ~7 μT upper limit is also consistent with our estimates of the expected stray remanent field produced by the underlying 12017 basalt at the

location of the glass rind. To calculate the remanent field produced by the underlying basalt, we followed the methodology of *Barnett* [1976]. We first created a triangular faceted three-dimensional digital model of the basalt portion of 12017 (Figure 10a) from a plaster cast made of the whole rock prior to subsampling at JSC. We assumed that the basalt was uniformly magnetized throughout its entire volume in the direction of the putative mean HC magnetization direction obtained with PCA (declination = 139.4°, inclination = 39.6°). We also assumed that the magnetization is that of a total TRM acquired in a paleofield given by our paleointensity upper limit of ~37 μT (section 5), which we estimated by scaling from our ARM acquisition measurements on the basalt with $f' = 1.34$. This corresponds to a magnetization of ~0.03 A/m. We then calculated the strength and direction of the external basalt field at the locations of our glass samples. In particular, following *Barnett* [1976], we relied on the fact that the magnetic potential at a point outside a uniformly magnetized volume can be expressed as an integral over the surface of the volume, which we approximated with triangular facets (Figure 10a). To estimate the uncertainty on the predicted field, we then repeated this calculation for different magnetization directions distributed within the 95% confidence interval of the mean HC magnetization (21°).

The results show that the measured directions of the glass are collectively incompatible with the magnetic field arising from the basalt according to our model (Figure 10b). The scatter in the magnetization directions predicted by the remanent field model does not encompass the wide range in HC directions observed in the glass (Figure 10b). In particular, the predicted field directions are only consistent with the computed HC directions in two of our four glass samples. Even more importantly, the predicted magnetic field intensity at the locations of the glass subsamples is only ~140 nT, comparable with the magnetic field in our shielded room and far less than the minimum retrievable paleointensity (~7 μT; see section 5). Therefore, remanent fields either from the large-scale crust at the Apollo 12 site (measured to be 36 nT) [*Dyal et al.*, 1970] or the underlying 12017 basalt are likely incapable of producing a TRM in the glass that would be recoverable using our AF methods. Additionally, if the regional crustal fields were to magnetize the glass rind, we would expect a roughly unidirectional magnetization.

8. Implications

We conclude that the magnetization of the young glass rind on 12017 is unlikely to be a TRM formed in either a lunar dynamo or lunar crustal fields exceeding <~7 μT. In fact, it is unlikely to be a record of ancient lunar fields at all and is instead mostly spontaneous magnetization formed in a near-zero field and/or spurious remanence introduced by laboratory AF demagnetization.

Crustal field intensities measured at the Apollo 12, 14, and 15 landing sites were generally <100 nT; the maximum surface field of 327 nT was measured at the Apollo 16 landing site [*Dyal et al.*, 1974]. This suggests that most of the high (1–20 μT) paleointensities previously inferred for other young (≤1.5 Ga) Apollo samples [see *Wieczorek et al.*, 2006, Figure 3.22] were also not produced by remanent crustal fields. Given that *Tikoo et al.* [2012, 2014] found no evidence for a lunar magnetic field >~4 μT by 3.19 Ga and that AF methods are incapable of accurately retrieving paleointensities <~20 μT for the vast majority of lunar samples (whose magnetic mineralogies are dominated by multidomain kamacite), it is likely that few—if any—of the ≤1.5 Ga Apollo era paleointensity determinations are accurate. Therefore, at present there is no evidence that lunar samples aged ≤3 Ga formed in the presence of >~4 μT magnetic fields from either a prolonged lunar core dynamo or meteoroid impacts.

9. Conclusions

1. Apollo 12 basalt 12017 is partially covered by an impact melt glass splash that formed <7 Ma. This glass is within error the youngest lunar sample studied with paleomagnetic methods.
2. The magnetization in both the 12017 glass and basalt is predominantly from a LC overprint acquired after sampling.
3. We could not identify a stable NRM carried by HC grains in either the basalt or glass lithologies of 12017. The magnetization in this range appears to be mostly a combination of spontaneous magnetization and spurious remanence introduced by the demagnetization process.
4. No fields likely stronger than ~37 μT were present at 3.35 Ga at the Apollo 12 site.
5. No fields likely stronger than ~7 μT were present at <7 Ma at the Apollo 12 site.
6. There is no evidence from sample 12017 for a core dynamo on the Moon at or after 3.35 Ga.

References

Barnett, C. (1976), Theoretical modeling of the magnetic and gravitational fields of an arbitrarily shaped three-dimensional body, *Geophysics*, *41*, 1353–1364, doi:10.1190/1.1440685.

Carporzen, L., and S. A. Gilder (2006), Evidence for coeval Late Triassic terrestrial impacts from the Rochechouart (France) meteorite crater, *Geophys. Res. Lett.*, *33*, L19308, doi:10.1029/2006GL027356.

Carporzen, L., B. P. Weiss, S. A. Gilder, A. Pommier, and R. J. Hart (2012), Lightning remagnetization of the Vredefort impact crater: No evidence for impact-generated magnetic fields, *J. Geophys. Res.*, *117*, E01007, doi:10.1029/2011JE003919.

Carslaw, H. S., and J. C. Jaeger (1959), *The Conduction of Heat in Solids*, Oxford Univ. Press, London.

Cisowski, S., J. Dunn, M. Fuller, Y. Wu, M. Rose, and P. Wasilewski (1976), Magnetic effects of shock and their implications for lunar magnetism. II, in *Proceedings of the Seventh Lunar Science Conference*, pp. 3299–3320, Pergamon, New York.

Cisowski, S., C. Hale, and M. Fuller (1977), On the intensity of ancient lunar fields, in *Proceedings of the Eighth Lunar Science Conference*, pp. 725–750, Pergamon, New York.

Cisowski, S., D. Collinson, S. Runcorn, A. Stephenson, and M. Fuller (1983), A review of lunar paleointensity data and implications for the origin of lunar magnetism, *J. Geophys. Res.*, *88*, A691–A704, doi:10.1029/JB088iS02p0A691.

Cournède, C., J. Gattacceca, and P. Rochette (2012), Magnetic study of large Apollo samples: Possible evidence for an ancient centered dipolar field on the Moon, *Earth Planet. Sci. Lett.*, *331*, 31–42, doi:10.1016/j.epsl.2012.03.004.

Crawford, D. A., and P. H. Schultz (1999), Electromagnetic properties of impact-generated plasma, vapor and debris, *Int. J. Impact Eng.*, *23*, 169–180, doi:10.1016/S0734-743X(99)00070-6.

Dunn, J., and M. Fuller (1972), On the remanent magnetism of lunar samples with special reference to 10048,55 and 14053,48, in *Proceedings of the Third Lunar Science Conference*, pp. 2363–2386, MIT Press, Cambridge.

Dwyer, C. A., D. J. Stevenson, and F. Nimmo (2011), A long-lived lunar dynamo driven by continuous mechanical stirring, *Nature*, *479*, 212–214, doi:10.1038/nature10564.

Dyal, P., C. W. Parkin, and C. P. Sonett (1970), Apollo 12 magnetometer: Measurement of a steady magnetic field on the surface of the Moon, *Science*, *169*, 762–764, doi:10.1126/science.169.3947.762.

Dyal, P., C. W. Parkin, and W. D. Daily (1974), Magnetism and the interior of the Moon, *Rev. Geophys. Space Phys.*, *12*, 568–591, doi:10.1029/RG012i004p00568.

Evans, A. J., M. T. Zuber, B. P. Weiss, and S. M. Tikoo (2014), A wet, heterogeneous lunar interior: Lower mantle and core dynamo evolution, *J. Geophys. Res. Planets*, *118*, 1061–1077, doi:10.1002/2013JE004494.

Fleischer, R. L., H. R. Hart, G. M. Comstock, and A. O. Evwaraye (1971), The particle track record of the Ocean of Storms, in *Proceedings of the Second Lunar Science Conference*, pp. 2559–2568, MIT Press, Cambridge, Mass.

Fuller, M., and S. M. Cisowski (1987), Lunar paleomagnetism, in *Geomagnetism*, vol. 2, edited by J. A. Jacobs, pp. 307–456, Academic Press, London.

Garrick-Bethell, I., B. P. Weiss, D. L. Shuster, and J. Buz (2009), Early lunar magnetism, *Science*, *323*, 356–359, doi:10.1126/science.1166804.

Gattacceca, J., and P. Rochette (2004), Toward a robust normalized magnetic paleointensity method applied to meteorites, *Earth Planet. Sci. Lett.*, *227*, 377–393, doi:10.1016/j.epsl.2004.09.013.

Gattacceca, J., M. Boustie, L. Hood, J. P. Cuq-Lelandais, M. Fuller, N. Bezaeva, T. de Resseguier, and L. Berthe (2010), Can the lunar crust be magnetized by shock: Experimental groundtruth, *Earth Planet. Sci. Lett.*, *299*, 42–53, doi:10.1016/j.epsl.2010.08.011.

Gose, W., D. Strangway, and G. Pearce (1973), A determination of the intensity of the ancient lunar magnetic field, *Earth Moon Planets*, *7*, 196–201, doi:10.1007/BF00578816.

Grove, T. L., and D. Walker (1977), Cooling histories of Apollo 15 quartz-normative basalts, in *Proceedings of the Eighth Lunar Science Conference*, pp. 1501–1520, Pergamon, New York.

Horn, P., T. Kirsten, and E. Jessberger (1975), Are there Apollo 12 mare basalts younger than 3.1 b.y. Unsuccessful search for Apollo 12 mare basalts with crystallization ages below 3.1 b.y, *Meteoritics*, *10*, 417.

Horz, F., and J. Hartung (1971), The lunar-surface orientation of some Apollo 12 rocks, in *Proceedings of the Third Lunar Science Conference*, pp. 2629–2638, MIT Press, Cambridge, Mass.

Horz, F., E. Schneider, D. Gault, J. Hartung, and D. Brownlee (1975), Catastrophic rupture of lunar rocks: A Monte Carlo simulation, *Moon*, *13*, 235–258, doi:10.1007/BF00567517.

Husain, L. (1974), ^{40}Ar-^{39}Ar chronology and cosmic ray exposure ages of the Apollo 15 samples, *J. Geophys. Res.*, *79*, 2588–2606, doi:10.1029/JB079i017p02588.

Kirschvink, J. L. (1980), The least-squares line and plane and the analysis of palaeomagnetic data, *Geophys. J. R. Astron. Soc.*, *62*, 699–718, doi:10.1111/j.1365-246X.1980.tb02601.x.

Kirschvink, J. L., R. E. Kopp, T. D. Raub, C. T. Baumgartner, and J. W. Holt (2008), Rapid, precise, and high-sensitivity acquisition of paleomagnetic and rock-magnetic data: Development of a low-noise automatic sample changing system for superconducting rock magnetometers, *Geochem. Geophys. Geosyst.*, *9*, Q05Y01, doi:10.1029/2007GC001856.

Laneuville, M., M. Wieczorek, D. Breuer, and N. Tosi (2013), Asymmetric thermal evolution of the Moon, *J. Geophys. Res. Planets*, *118*, 1435–1452, doi:10.1002/jgre.20103.

Laneuville, M., M. A. Wieczorek, D. Breuer, J. Aubert, G. Morard, and T. Ruckriemen (2014), A long-lived lunar dynamo powered by core crystallization, *Earth Planet. Sci. Lett.*, *401*, 251–260, doi:10.1016/j.epsl.2014.05.057.

Lawrence, K., C. Johnson, L. Tauxe, and J. Gee (2008), Lunar paleointensity measurements: Implications for lunar magnetic evolution, *Phys. Earth Planet. Inter.*, *168*, 71–87, doi:10.1016/j.pepi.2008.05.007.

Le Bars, M., M. A. Wieczorek, Ö. Karatekin, D. Cébron, and M. Laneuville (2011), An impact-driven dynamo for the early Moon, *Nature*, *479*, 215–218, doi:10.1038/nature10565.

Louzada, K. L., B. P. Weiss, A. C. Maloof, S. T. Stewart, N. L. Swanson-Hysell, and S. A. Soule (2008), Paleomagnetism of Lonar impact crater, India, *Earth Planet. Sci. Lett.*, *275*, 308–319, doi:10.1016/j.epsl.2008.08.025.

Morgan, J. W., J. Laul, R. Ganapathy, and E. Anders (1971), Glazed lunar rocks: Origin by impact, *Science*, *172*, 556–558, doi:10.1126/science.172.3983.556.

Morrison, D., D. McKay, G. Heiken, and H. Moore (1972), Microcraters on lunar rocks, in *Proceedings of the Third Lunar Science Conference*, pp. 2767–2791, MIT Press, Cambridge, Mass.

Pearce, G., W. Gose, and D. Strangway (1973), Magnetic studies on Apollo 15 and 16 lunar samples, in *Proceedings of the Fourth Lunar Science Conference*, pp. 3045–3076, Pergamon, Elmsford, N. Y.

Scheinberg, A., K. M. Soderlund, and G. Schubert (2015), Magnetic field generation in the lunar core: The role of inner core growth, *Icarus*, *254*, 62–71, doi:10.1016/j.icarus.2015.03.013.

Schultz, P. H., and P. D. Spudis (1983), Beginning and end of lunar mare volcanism, *Nature, 302*, 233–236, doi:10.1038/302233a0.

Sclar, C. (1971), Shock-induced features of Apollo 12 microbreccias, in *Proceedings of the Second Lunar Science Conference*, pp. 160–163, MIT Press, Cambridge, Mass.

Shea, E. K., B. P. Weiss, W. S. Cassata, D. L. Shuster, S. M. Tikoo, J. Gattacceca, T. L. Grove, and M. D. Fuller (2012), A long-lived lunar core dynamo, *Science, 335*, 453–456, doi:10.1126/science.1215359.

Shuster, D. L., and W. S. Cassata (2015), Paleotemperatures at the lunar surfaces from open system behavior of cosmogenic ^{38}Ar and radiogenic ^{40}Ar, *Geochim. Cosmochim. Acta, 155*, 154–171, doi:10.1016/j.gca.2015.01.037.

Shuster, D. L., G. Balco, W. S. Cassata, V. A. Fernandes, I. Garrick-Bethell, and B. P. Weiss (2010), A record of impacts preserved in the lunar regolith, *Earth Planet. Sci. Lett., 290*, 155–165, doi:10.1016/j.epsl.2009.12.016.

Srnka, L., G. Martelli, G. Newton, S. Cisowski, M. Fuller, and R. Schaal (1979), Magnetic field and shock effects and remanent magnetization in a hypervelocity impact experiment, *Earth Planet. Sci. Lett., 42*, 127–137, doi:10.1016/0012-821X(79)90198-5.

Stephenson, A. (1993), Three-axis static alternating field demagnetization of rocks and the identification of natural remanent magnetization, gyroremanent magnetization, and anisotropy, *J. Geophys. Res., 98*, 373–381, doi:10.1029/92JB01849.

Stephenson, A., and D. Collinson (1974), Lunar magnetic field palaeointensities determined by an anhysteretic remanent magnetization method, *Earth Planet. Sci. Lett., 23*, 220–228, doi:10.1016/0012-821X(74)90196-4.

Strangway, D., G. Pearce, W. Gose, and R. Timme (1971), Remanent magnetization of lunar samples, *Earth Planet. Sci. Lett., 13*, 43–52, doi:10.1016/0012-821X(71)90103-8.

Suavet, C., B. P. Weiss, W. S. Cassata, D. L. Shuster, J. Gattacceca, L. Chan, I. Garrick-Bethell, J. W. Head, T. L. Grove, and M. D. Fuller (2013), Persistence and origin of the lunar core dynamo, *Proc. Natl. Acad. Sci. U.S.A., 110*, 8453–8458, doi:10.1073/pnas.1300341110.

Sugiura, N., and D. Strangway (1980), Comparisons of magnetic paleointensity methods using a lunar sample, in *Proceedings of the Eleventh Lunar and Planetary Sciences Conference*, pp. 1801–1813, Pergamon, New York.

Sugiura, N., D. Strangway, G. Pearce, Y. Wu, and L. Taylor (1979), A new magnetic paleointensity value for a "young lunar glass", in *Proceedings of the Tenth Lunar Science Conference*, pp. 2189–2197, Pergamon, New York.

Tauxe, L., and H. Staudigel (2004), Strength of the geomagnetic field in the Cretaceous Normal Superchron: New data from submarine basaltic glass of the Troodos Ophiolite, *Geochem. Geophys. Geosyst., 5*, Q02H06, doi:10.1029/2003GC000635.

Tian, B. Y., S. Stanley, S. M. Tikoo, and B. P. Weiss (2014), A precession-driven lunar dynamo, paper presented at AGU Fall Meeting, GP54A-04, AGU, San Fransisco, Calif.

Tikoo, S. M., B. P. Weiss, J. Buz, E. A. Lima, E. K. Shea, G. Melo, and T. L. Grove (2012), Magnetic fidelity of mare basalts and implications for a lunar dynamo, *Earth Planet. Sci. Lett., 337–338*, 93–103, doi:10.1016/j.epsl.2012.05.024.

Tikoo, S. M., B. P. Weiss, W. S. Cassata, D. L. Shuster, J. Gattacceca, E. A. Lima, C. Suavet, F. Nimmo, and M. D. Fuller (2014), Decline of the lunar core dynamo, *Earth Planet. Sci. Lett., 404*, 89–97, doi:10.1016/j.epsl.2014.07.010.

Warner, J. (1970), *Apollo 12 Lunar Sample Information*, NASA Curatorial Branch Publ., Houston.

Weisberg, S. (1985), *Applied Linear Regression*, John Wiley, New York.

Weiss, B. P., and S. M. Tikoo (2014), The lunar dynamo, *Science, 346*, doi:10.1126/science.1246753.

Weiss, B., S. Pedersen, I. Garrick-Bethell, S. Stewart, K. Louzada, A. Maloof, and N. Swanson-Hysell (2010), Paleomagnetism of impact spherules from Lonar crater, India and a test for impact-generated fields, *Earth Planet. Sci. Lett., 298*, 66–76, doi:10.1016/j.epsl.2010.07.028.

Wieczorek, M. A., B. L. Jolliff, A. Khan, M. E. Pritchard, B. P. Weiss, J. G. Williams, L. L. Hood, K. Righter, C. R. Neal, and C. K. Shearer (2006), The constitution and structure of the lunar interior, *Rev. Mineral. Geochem., 60*, 221, doi:10.2138/rmg.2006.60.3.

Zhang, N., E. Parmentier, and Y. Liang (2013), A 3-D numerical study of the thermal evolution of the Moon after cumulate mantle overturn: The importance of rheology and core solidification, *J. Geophys. Res. Planets, 118*, 1789–1804, doi:10.1002/jgre.20121.

Magnetism of a Very Young Lunar Glass

Jennifer Buz[1*], Benjamin P. Weiss[1], Sonia M. Tikoo[2,3], David L. Shuster[2,3], Jérôme Gattacceca[4], Timothy L. Grove[1]

[1]Department of Earth, Atmospheric, and Planetary Sciences, Massachusetts Institute of Technology, Cambridge, MA 02139, USA, [2]Department of Earth and Planetary Science, University of California, Berkeley, CA 94720, USA., [3]Berkeley Geochronology Center, Berkeley, CA 94709, USA, [4]CNRS, Aix-Marseille University, CEREGE UM 34, Aix-en-Provence, France, *Now at: Division of Geological and Planetary Sciences, California Institute of Technology, Pasadena, CA 91125

Contents of this file

Additional Supporting Information (Files uploaded separately)

Introduction

This supporting information provides additional details on hysteresis, VRM, PRM, geo- and thermochronometry experiments. Demagnetization data for all samples are included in the supplementary figures if not in the main text. Additional elucidating figures and tables are also provided. Demagnetization data is provided in the supplementary dataset.

Text S1. Rock Magnetism of 12017

1.1 Hysteresis

Hysteresis loops were measured on a single sample of each the 12017 basalt and glass lithologies using a Princeton Instruments MicroMag vibrating sample magnetometer at CEREGE, Aix-en-Provence, France. Hysteresis data are shown in Fig. S1. Magnetic hysteresis parameters are reported in Tikoo et al [2012]. Using the hysteresis data with the diamagnetic and paramagnetic contributions subtracted, we estimated the saturation remanence, saturation magnetization, and coercivity. The ratios of saturation remanence to saturation magnetization (M_{rs}/M_s) for basalt and glass are 5.05×10^{-3} and 3.89×10^{-3}, respectively. The mass normalized M_s are 0.14 Am^2/kg and 0.68 Am^2/kg for the basalt and glass, respectively. The ratios of remanent coercive force to coercive force (H_{cr}/H_c) are 17.5 and 5.67 for basalt and glass, respectively. Using these parameters as well as the coercivity of remanence determined from back field IRM experiments, we find that both lithologies are dominated by multidomain grains.

1.2 VRM

A possible source of magnetization for 12017 is viscous remanent magnetization (VRM) from exposure to the Earth's magnetic field for 40 years at ambient temperatures. To estimate the possible contribution of VRM on the magnetization of the samples, we placed basalt sample 13B in the Earth's magnetic field for 2 weeks and we placed glass sample 12B in an artificial bias field of 0.2 mT generated by a coil inside our shielded room for 21 hours. Upon removal of the applied field, we acquired continuous measurements of the magnetization of the samples as they viscously relaxed in our shielded room (< 200 nT) over the following two weeks. To estimate lower and upper bounds on the amount of possible VRM acquired since arrival on Earth, we fit both linear and exponential curves to the VRM decay data, respectively (Fig. S2). We extrapolated the acquired remanence out to 40 years (approximate residence time on Earth) and subtracted the decay time from being in our shielded room (approximately 1 year). Linear fits suggest that VRM can account for 1.95% and 0.5% of the basalt and glass NRM, respectively, and 1.7% and 1.8% of the LC component. Exponential fits suggest that VRM can account for 10% and 11% of the basalt and glass NRM, respectively, and 21% and 34% of the LC component. These are actually all upper limits since they assume that the samples were stationary in the Earth's field over the last 40 years.

1.3 PRM

It is possible that the glass or basalt could have acquired a shock remanent magnetization (SRM) from a meteoroid impact. It is important to consider this because SRM is capable of recording very short lived fields like putative impact-plasma generated fields [*Crawford and Schultz*, 1999]. To assess this possibility, we imparted a laboratory pressure remanent magnetization (PRM) (as an analog for SRM) on basalt sample 12A2 following the methods of Gattacceca et al. [2010]. We immersed sample 12A2 in polyethilsiloxane fluid to facilitate hydrostatic pressurization. We then put the capsule containing the sample and fluid into a nonmagnetic pressure cell and raised the pressure to 1.8 GPa. While maintaining this pressure for a minimum of 1 minute, we applied a field of 800 μT using a coil wrapped around the cell. The field was then turned off, the

pressure removed over the course of a minute, and the sample subjected to a full AF demagnetization sequence. A comparison of demagnetization of PRM with NRM is shown in Figs. S5 and S7. Almost all of the magnetization acquired via PRM was removed in the first AF step (20 mT), suggesting that even the LC component is too hard to be explained as an SRM.

Text S2. ^{40}Ar/^{39}Ar and cosmogenic ^{38}Ar geochronology analytical details

Two basalt aliquots of 12017 and a single aliquot of 12017 impact glass were sequentially degassed to conduct ^{40}Ar/^{39}Ar geochronometry at the Berkeley Geochronology Center following previously published procedures [*Shea et al.*, 2012; *Shuster et al.*, 2010]. The basalt samples were placed into aluminum discs alongside Hb3gr neutron fluence monitors and were irradiated for 100 hours, and the glass aliquot was irradiated for 1 hour alongside ACs fluence monitors, at the Oregon State University TRIGA reactor in the Cadmium-Lined In-Core Irradiation Tube (CLICIT) facility. After irradiation, aliquots (~1 mg) of the irradiated basalt and glass were placed into small metal tubes of high purity Pt-Ir alloy and incrementally degassed using feedback-controlled laser heating with a 30 W diode laser (wavelength of 810 ± 10 nm) equipped with a coaxially aligned optical pyrometer. The single-color pyrometer was calibrated against a type-K thermocouple under high vacuum ($<10^{-8}$ torr) and under the same conditions as the degassing analyses to correct for the temperature dependent emissivity of the Pt-Ir tubes.

During sequential degassing, the samples were first held under static vacuum at a controlled temperature to within $\pm 10°C$ for 600 s (Table S1). The extracted Ar was then purified using one hot and one cold SAES® GP-50 getter pump fitted with C-50 cartridge (St101 alloy). All five isotopes of Ar were analyzed with a Mass Analyzer Products 215c mass spectrometer using a single Balzers SEV-217 discrete dynode electron multiplier. Corrections for interfering nuclear reaction products [*Renne et al.*, 2005], ^{37}Ar and ^{39}Ar decay, spectrometer discrimination, and extraction line blanks were applied to the measured signals. Apparent ^{40}Ar/^{39}Ar ages were calculated relative to the Hb3gr standard (1081 Ma) or the ACs standard (1.206 Ma) using the decay constants and standard calibration of Renne et al. [2011], and isotope abundances of Steiger and Jäger [1977]; corrections for trapped or cosmogenic ^{40}Ar were not applied. The apparent cosmogenic ^{38}Ar exposure ages of each degassing step were calculated from the ratio of cosmogenic ^{38}Ar to reactor-produced ^{37}Ar and ^{39}Ar following the procedures described in Shuster and Cassata [2015] and using the ^{38}Ar production rate from Ca [*Turner*, 1971]. In this case, the production of ^{38}Ar$_{cos}$ from Ti, Cr, Mn, Fe, and Ni was ignored; therefore, calculated exposure ages represent upper bounds on the true surface exposure. Full datasets, isotopic corrections, neutron irradiation parameters, and calculated step ages (both ^{40}Ar/^{39}Ar and cosmogenic ^{38}Ar) for the whole-rock and glass aliquots appear in Table S1. For the analysis of impact glass, extractions that yielded Ar abundances below the detection limit are excluded for clarity. The whole-rock analyses are shown as release spectra, along with the apparent Ca/K ratios, in Fig. 7.
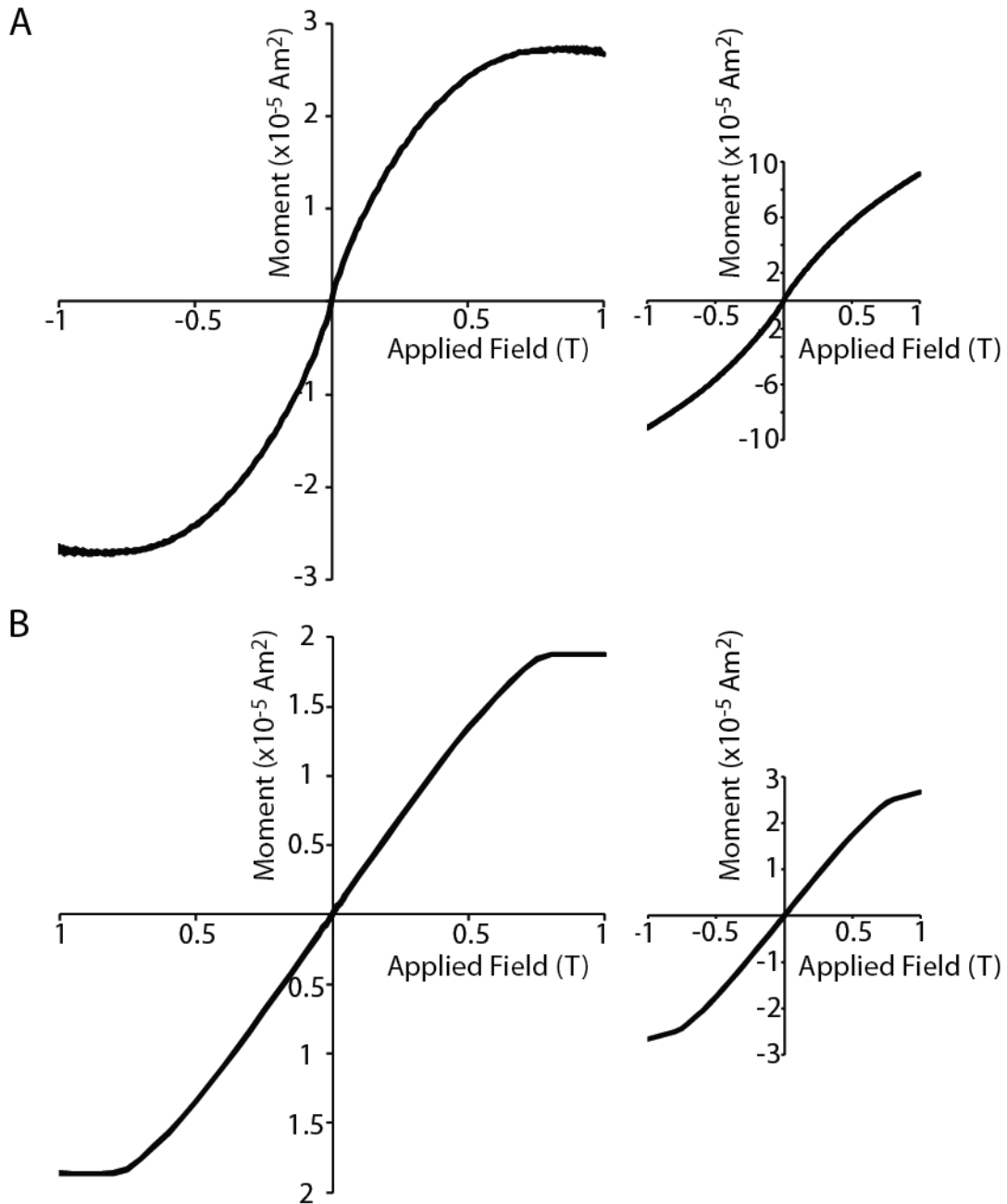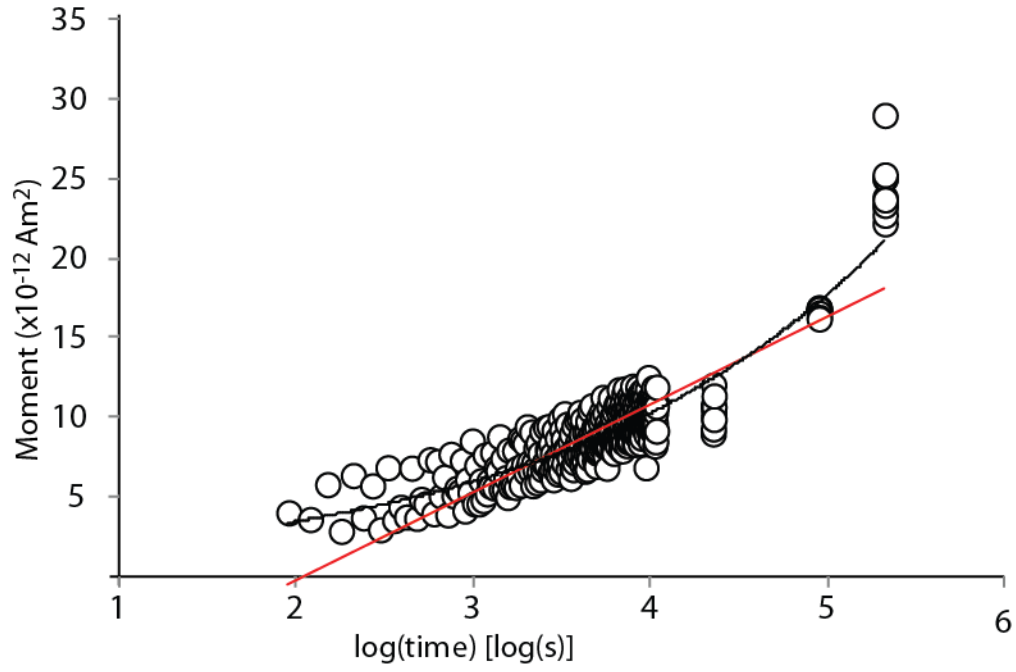
Figure S1. Hysteresis data for 12017. A) Basalt subsample 12A2. B) Glass subsample 12B. Large plots at left show hysteresis loops corrected for high-field (0.95-1 T) paramagnetic slope while the smaller plots at right show the uncorrected data.
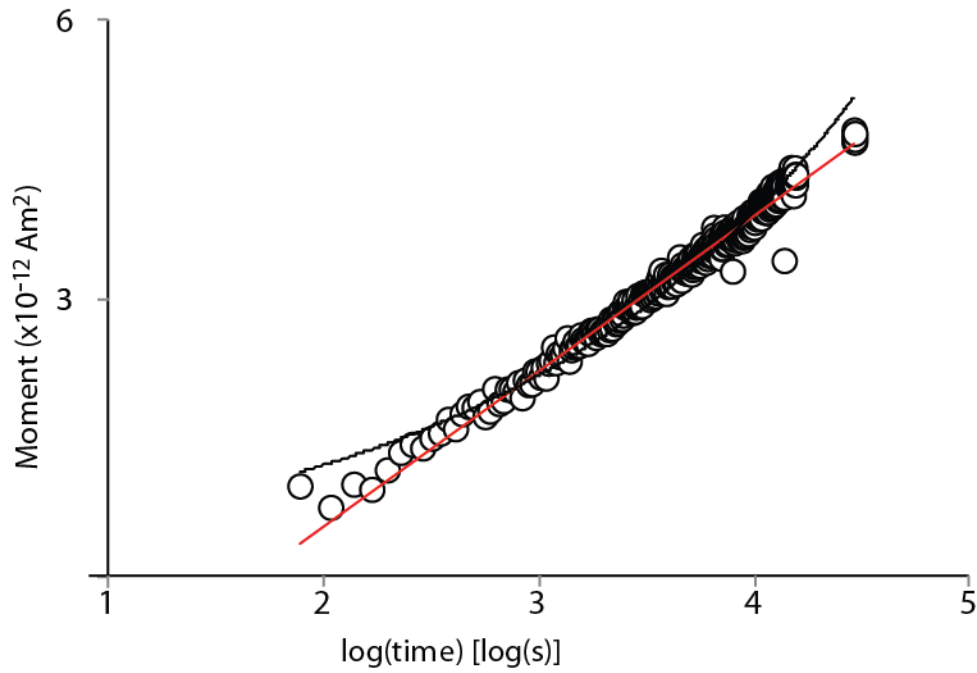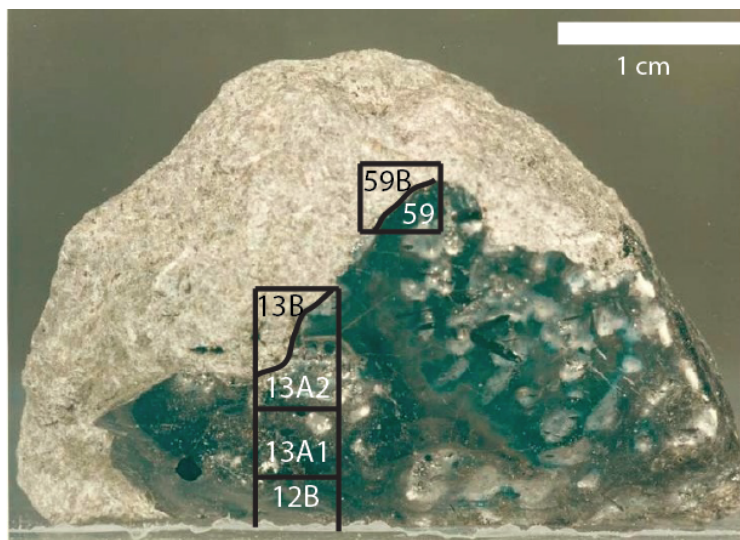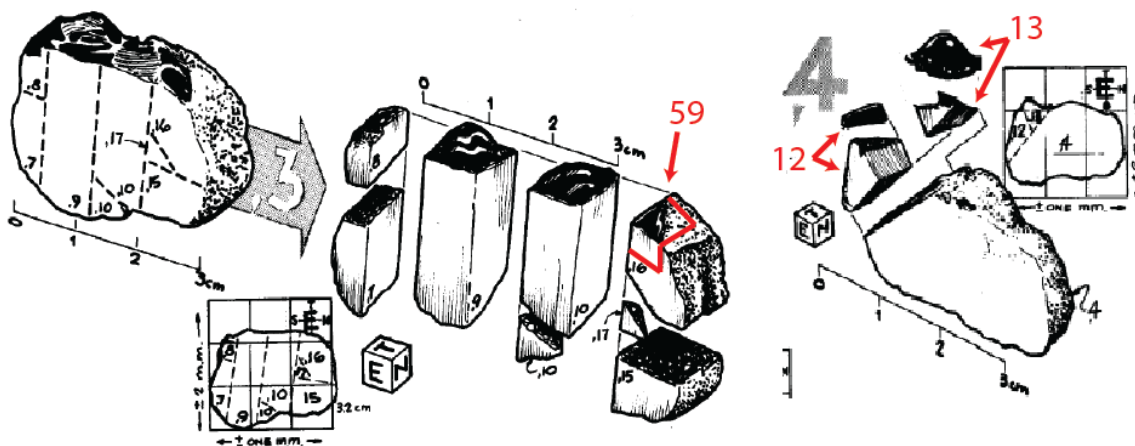
A

B

Figure S2. VRM decay experiments for 12017. (A) Basalt subsample 13B1. (B) Glass subsample 12B. Black lines indicate exponential fits while red lines indicate linear fits.

A

59B
59

13B
13A2
13A1
12B

1 cm

B

3

59

4

13

12

C

W W'

13A2
12B
13A1
glass
glass
basalt
59A
basalt
13B
12A2
12A1A
12A1C
12A1B
59B

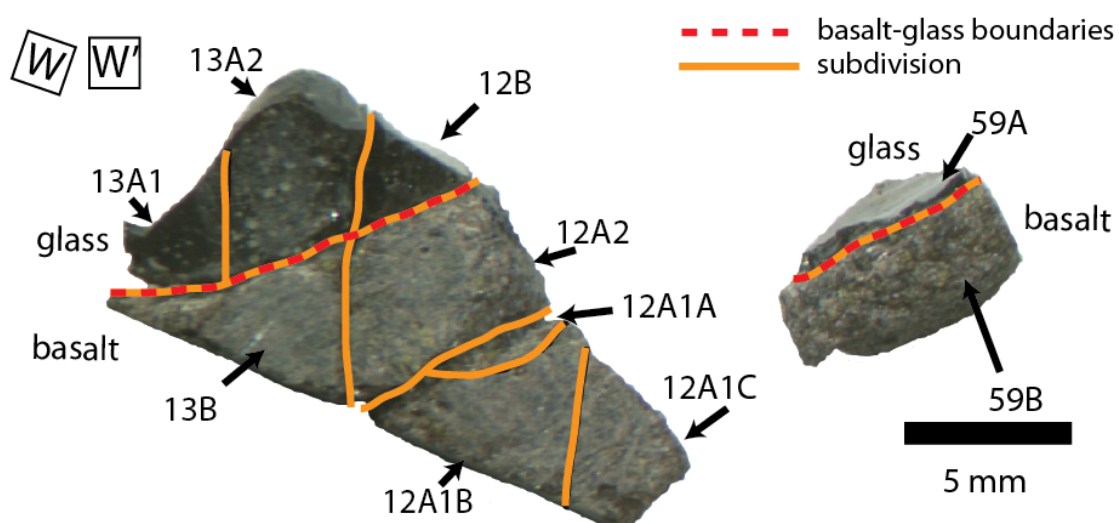basalt-glass boundaries
subdivision

5 mm

Figure S3. Subsampling and orientation of 12017. A) Whole rock 12017 prior to subdivision at Johnson Space Center (JSC). Underlying basalt is light gray and glass splatter is shiny black. Approximate locations of subsamples used in this study are indicated. NASA photo S70-44098. B) Illustration of saw cuts made at JSC during sample processing, adapted from Lunar Sample Compendium [*Meyer*, 2005]. We used these drawings to reconstruct how our allocated subsamples were mutually oriented. C) Orientation of final subsamples used in this study. Subsamples 12A1A, 12A1B, and 59B were not used in this study. The JSC and MIT coordinate systems are shown with unprimed and primed labels, respectively, in (B) and (C).

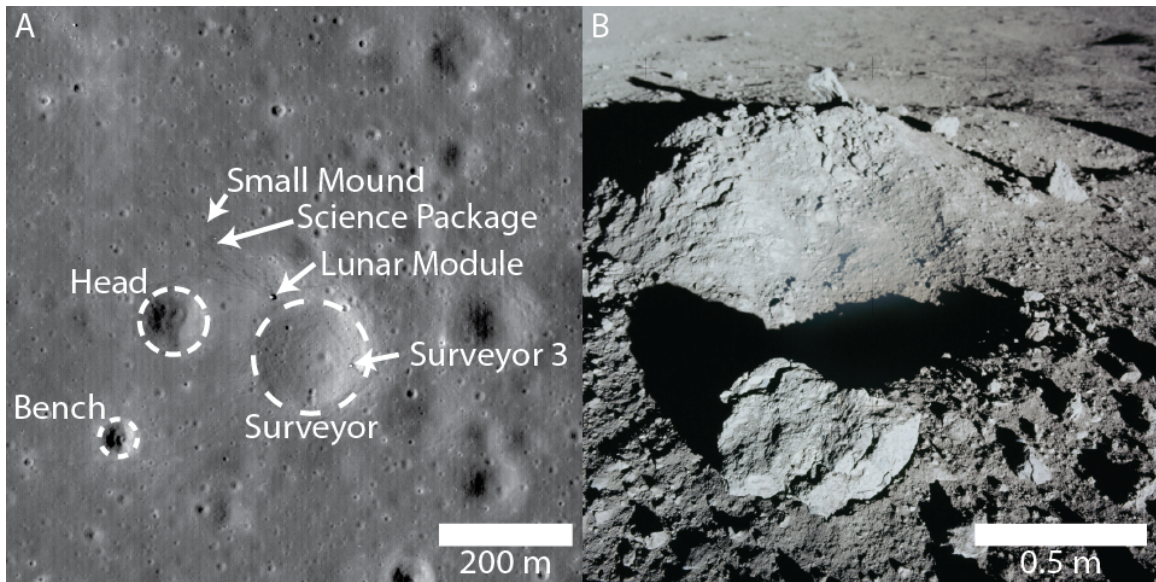**Figure S4.** Geologic setting of 12017. A) Lunar Reconnaissance Orbiter Wide Angle Camera (LROC-WAC) photograph of the Apollo 12 landing site. Selected craters and the small mound where sample 12017 was thought to have been collected are labeled. B) Astronaut photograph (AS12-46-6825HR) of small mound where sample 12017 was retrieved (sample is not identifiable in the photograph). Scale bar is estimated from the Apollo transcripts.
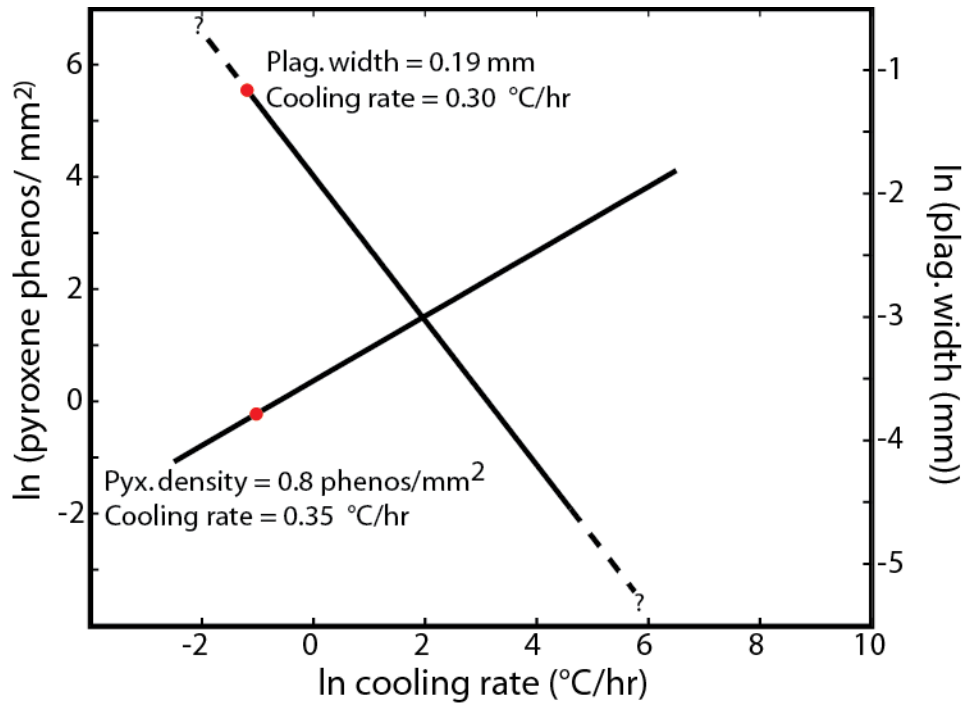
Figure S5. Petrographic constraints on cooling rate of 12017 basalt from Grove and Walker [1977]. Early and late stage cooling of the 12017 basalt based on plagioclase width and pyroxene density are 0.30°C/hr and 0.35°C/hr, respectively. See Fig. 1 for examples of plagioclase and pyroxene.
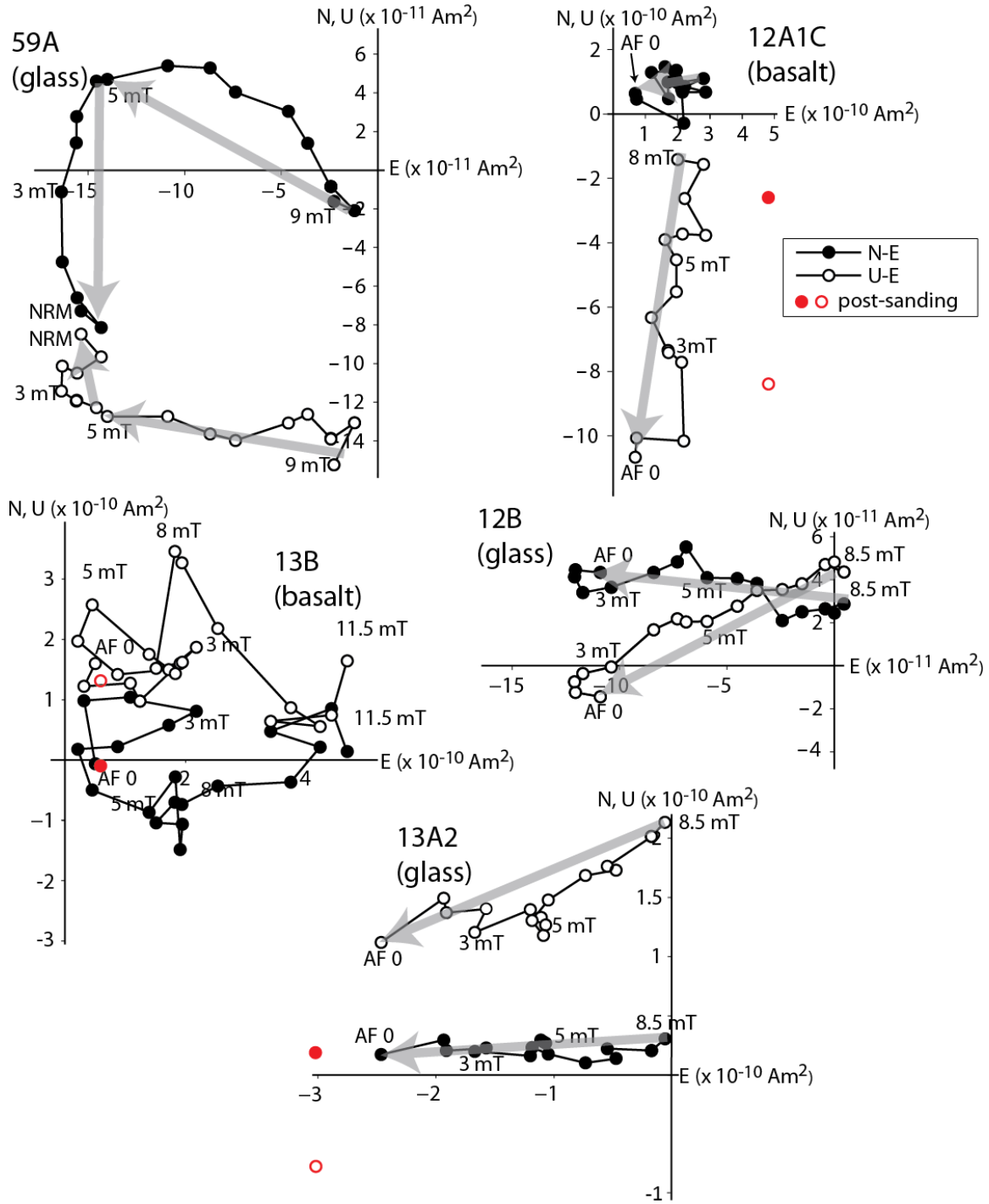
Figure S6. More examples of AF demagnetization over the coercivity range of the LC component. Shown is a two-dimensional projection of the NRM vectors during progressive sanding stages. Solid symbols represent the end points of magnetization projected onto the horizontal N-E planes, and open symbols represent projections onto the vertical U-E planes. All samples except sample 13B show removal of one or more LC components. Sample 59A likely has two LC components, indicated by the grey arrows. Red symbols indicate moment measurement following final sanding of the

parent sample for each subsample show here and scaled in intensity to the mass of the subsample relative to its parent sample. These directions differ from the AF 0 mT measurements because of the additional subsampling that occurred prior to beginning AF demagnetization.
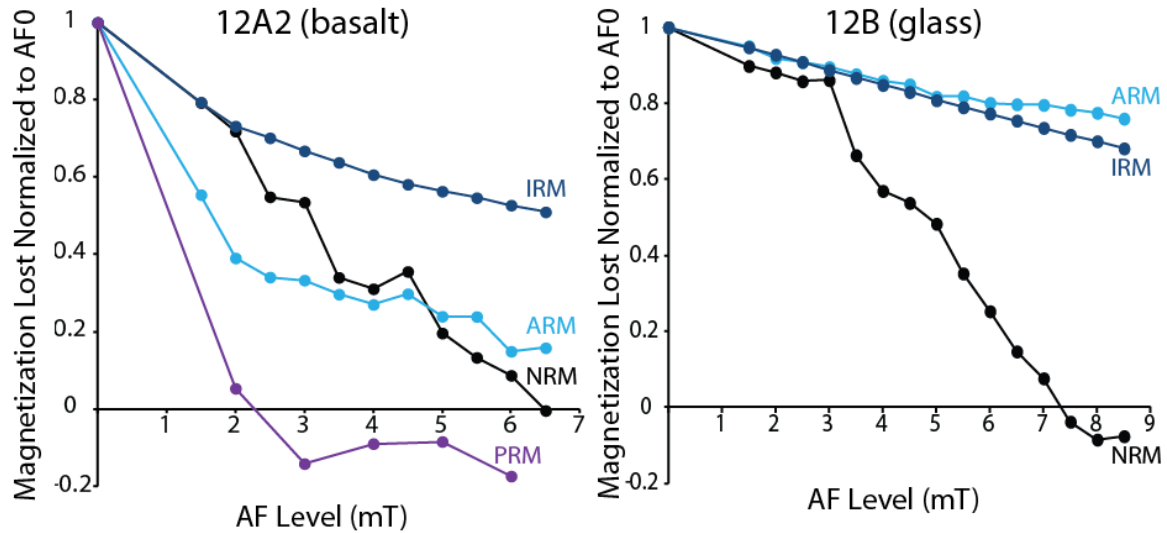
Figure S7. Comparison of AF demagnetization behavior of the NRM to that of different laboratory-induced magnetizations over the coercivity range of the LC component. (Left) 12A2 basalt subsample demagnetization normalized to the pre-AF moment. (Right) 12B glass subsample demagnetization normalized to the pre-AF moment.
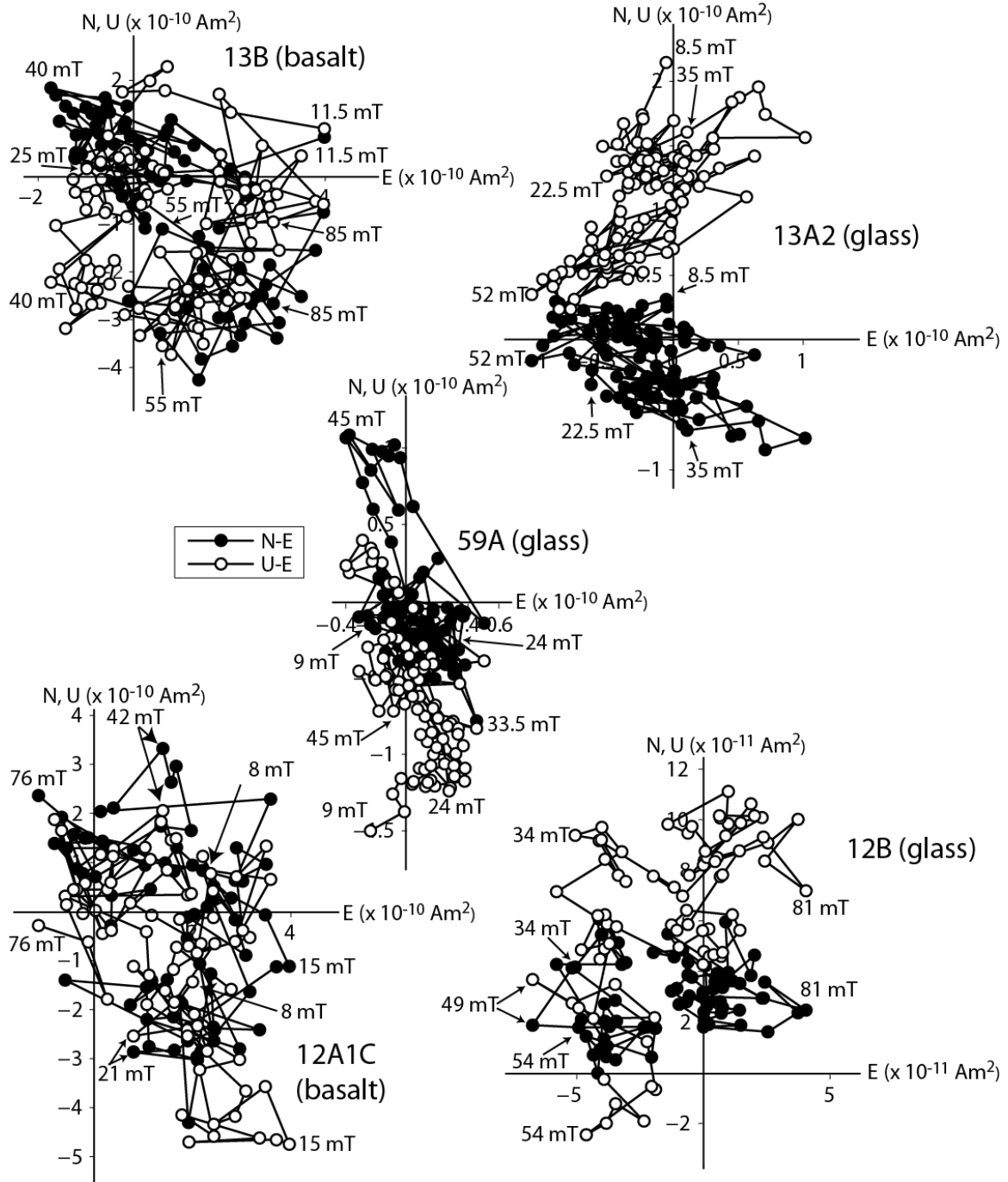
Figure S8. More examples of AF demagnetization of 12017 over the HC range. Shown is a two-dimensional projection of the NRM vectors during progressive sanding stages. Solid symbols represent the end points of magnetization projected onto the horizontal N-E planes, and open symbols represent those projected onto the vertical U-E planes. Note the lack of any consistent moment or directional changes with successive AF steps.

Figure S9. Comparison of AF demagnetization behavior for different magnetization types over the coercivity range of the HC magnetization. (Left) 12A2 basalt subsample normalized to the moments after demagnetization to 6.5 mT. (Right) 12B glass subsample normalized to the moments after demagnetization to 8.5 mT.
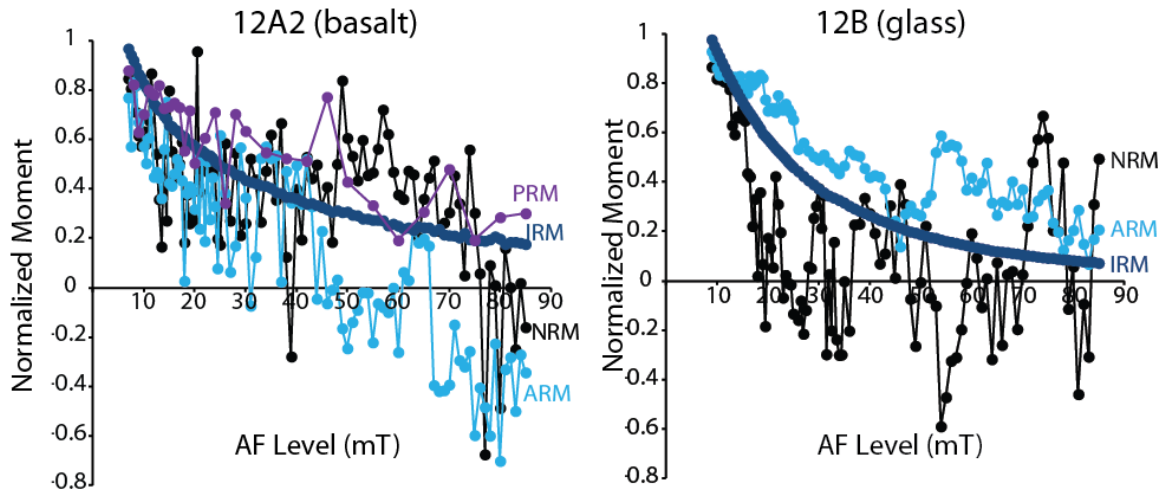
Isotope abundances given in nanoamps (spectrometer sensitivity is ~1.4×10^{-14} mols/nA), and corrected for ^{37}Ar and ^{39}Ar decay, half lives of 35.2 days and 269 years, respectively, and for spectrometer discrimination per atomic mass unit of 1.004535 ± 0.002968. Isotope sources calculated using the reactor constants in Renne et al. [1998], assuming (^{38}Ar/^{36}Ar)$_{cos}$ = 1.54, (^{38}Ar/^{36}Ar)$_{trap}$ = 0.188, and (^{40}Ar/^{36}Ar)$_{trap}$ = 0.

No corrections were made for cosmogenic ^{40}Ar. Ages calculated using the decay constants and standard calibration of Renne et al. [2011] and isotope abundances of Steiger and Jäger [1977] and calculated relative to Hb3gr fluence monitor (1081 Ma) and relative to ACs fluence monitor (1.206 Ma), for basalt and glass, respectively.

J-Values are 0.0262509 ± 0.0002064 and 0.000272 ± 0.000008, for basalt and glass respectively.

Corrections were made for reactor produced ^{38}Ar and ^{36}Ar in age calculations.

Average analytical blanks are: ^{40}Ar = 0.015; ^{39}Ar = 0.0001; ^{38}Ar = 0.00002; ^{37}Ar = 0.0001; ^{36}Ar = 0.00007 (nanoamps).

Temperature was controlled with approximately ± 10 $^{\circ}$C precision and ± 10 $^{\circ}$C accuracy; each heating duration was 600 seconds.

The apparent ^{38}Ar exposure ages are calculated for production only from Ca and K, so represent upper bounds.

Table S1. **Argon Analytical Details.**

#	Lithology	P	Ni	S	Fe	Total
1	Glass	0.16	0	0.11	16.53	16.80*
2	Glass	2.53	1.28	0.02	96.21	100.04
3	Glass	8.22	1.97	0.39	88.58	99.16
4	Glass	4.18	1.45	0.38	93.35	99.36
5	Glass	7.44	1.52	9.70	80.39	99.05
1	Basalt	0.01	0	0.25	98.99	99.25
2	Basalt	0.01	0	0.06	98.93	99.00
3	Basalt	0.02	0.79	0.01	97.58	98.40
4	Basalt	0.02	0.78	0.01	99.45	100.28

Note: The first column lists the spot number corresponding to Fig. 2, the second column lists the lithology hosting the metal grain. The second through fourth columns contain the concentrations in wt.% of P, Ni, S, and Fe, respectively. The fifth column contains the sum the previous four columns. Measurements were acquired with a JEOL-JXA-8200 at the Massachusetts Institute of Technology electron microprobe facility.

*The low mass percentage total for this spot is likely due to the small size (<1 μm) of this metal grain. The remaining majority of the mass is likely from Si and O from the surrounding glass.

Table S2. **Wavelength dispersive spectroscopy analyses of metal grains in 12017.**

Sample	Mass (mg)	Type	Range (mT)	N	Dec (°)	Inc (°)	DANG (°)	MAD (°)	Pass?	Forced?
Basalt										
12A	503	Sanding	-	6	249	-38.8		27.2		No
12A2	183	LC	NRM-8.5	17	294.5	33.7	127.1	12.0	N	No
		HC	8.5-69	77	145.7	48.1	74.26	37.1	N	Yes
12A1C	104.3	LC	NRM-8.0	15	239.9	81.0	151.6	11.0	N	No
		HC	8.0-64	74	127.0	42.6	132.1	35.3	N	Yes
13B*	131.6	Sanding	-	13	135.6	36.2		23.3		No
		LC	NRM-11.5	22	263.8	-17.4	124.6	36.3	N	No
		MC	12.0-54.0	66	121.0	-70.7	146.6	35.4	N	No
		HC	54-80	27	144.9	26.9	91.01	34.0	N	Yes
Glass										
12B	27.1	Sanding	n/a	5	348.8	66.2		24		No
		LC	NRM-8.5	16	277.8	24.7	133.7	9.8	N	No
		HC	9-85	75	346.8	-65.1	38.5	31.8	N	Yes
13A	132.9	Sanding	n/a	14	4.8	-7.6		27.2		No
13A1	69.9	LC	NRM-7	13	302.8	16.8	129.7	6.1	N	No
		HC	7.5-85	106	209	17.7	159.6	34.9	N	Yes
13A2	49.5	LC	NRM-8.5	16	269.9	21.1	106.2	14.0	N	No
		HC	8.5-85	104	206.4	-78.6	52.51	30.0	N	Yes
59A**	15	LC1	NRM-4.5	7	180	-11.4	91.63	9.4	N	No
		LC2***	5.0-9.0	9	303.6	-3.9	110.9	15.8	N	No
		HC	9.5-39	56	146.5	74.6	114.5	45.5	N	Yes

Note: The first column contains sample and subsample names. Subsamples are listed as indented sample names under their parent sample. The second column shows the mass of each subsample. The third column designates whether the row describes the low coercivity (LC), medium (MC), or high coercivity (HC) components of magnetization in the sample. The fourth column contains the AF field values bounding the components identified for each subsample. The fifth column shows the number of points (i.e., AF steps) used in the PCA calculation for each component. Columns 6-9 show the mean declination, mean inclination, DANG, and the MAD, respectively, for each component. The tenth column indicates whether the component passed the DANG/MAD test. The eleventh column indicates whether the component was forced through the origin during the PCA calculation. *In Tikoo et al. [2012] sample 13B was referred to as sample 13b1. **In Tikoo et al. [2012] sample 59A was referred to as sample 59. ***In Tikoo et al. [2012] component LC2 was referred to as MC.

Table S3. **NRM components.**

Sample	Starting Mass (mg)	Ending Mass (mg)	% Difference
12A	503.7	492.5	2.3
12B	32.2	29.7	7.7
13A	150.7	149.0	1.1
13B	167.2	152.1	9.0

Note: A ~20 mg flake of glass was chipped from 13B post-sanding.

Table S4. **Mass changes throughout sanding.**

Sample	Comp	ARM slope			IRM slope	ARM paleointensity (µT)			IRM
		0.05 mT	0.2 mT	0.6 mT		0.05 mT	0.2 mT	0.6 mT	Paleoint (µT)
Basalt 12A2	LC	2.71 ± 1.55	1.03 ± 0.19	0.45 ± 0.08	0.057 ± 0.0062	101.1 ± 57.8	153.73 ± 28.35	201.4 ± 35.82	171 ± 18.6
	HC	0.13± 0.13	0.12 ± 0.06	0.05 ± 0.03	0.0044 ± 0.003	4.104 ± 4.85	16.41 ± 8.95	22.38 ± 13.43	13.2 ± 9
12A1C	LC	1.53 ± 0.64	0.9 ± 0.13	0.5 ± 0.08	-	57.08 ± 23.88	134.32 ± 19.40	223.88 ± 35.82	-
	HC	0.14 ± 0.17	0.08 ± 0.09	0.03 ± 0.06	-	5.223 ± 6.34	11.94 ± 13.43	13.43 ± 26.86	-
Glass 12B	LC	3.93 ± 1.24	1.11 ± 0.11	0.33 ± 0.04	0.986 ± 0.11*	146.6 ± 46.26	165.67 ± 16.41	147.76 ± 17.91	295.8 ± 33.3
	HC	0.17 ± 0.07	0.05 ± 0.02	0.02 ± 0.01	0.004 ± 0.001*	6.343 ± 2.61	7.46 ± 2.98	8.95 ± 4.47	13.03 ± 3.94
13A2	LC	0.85 ± 0.86	0.39 ± 0.19	0.14 ± 0.06	0.007 ± 0.003*	31.71 ± 32.08	58.20 ± 28.35	62.68 ± 26.86	22.05 ± 8.40
	HC	0.24 ± 0.04	0.10 ± 0.01	0.04 ± 0.01	0.002 ± 0.0003*	8.955 ± 1.49	14.92 ± 1.49	17.91 ± 4.47	7.20 ± 0.99

Note: The first column lists subsample numbers. The second column designates whether the paleointensity experiment was conducted for the low coercivity (LC) component, high coercivity (HC) component, or a magnetization component defined by AF steps of 23-85 mT in the sample. The third, fourth, and fifth columns show ΔNRM/ΔARM values computed from paleointensity slope fits to the associated AF range using ARM acquisition with 0.05 mT, 0.2 mT, and 0.6 mT DC bias fields, respectively. The sixth column shows ΔNRM/ΔIRM values computed from paleointensity slope fits to the associated AF range. All data reported are in the format slope ± 95% formal confidence radius from Student's t-test. The final four columns indicate the calculated paleointensity using $f' = 1.34$ and $a = 3000$. The first six columns are reproduced from Tikoo et al. [2012]. The quoted uncertainties in the third through eight columns only represents that associated with the linear regression and does not take into account systematic uncertainties associated with the unknown values of a and f'. *Tikoo et al. [2012] incorrectly reported IRM paleointensities for subsample 12B as belonging to 13A2. They have been corrected here.
Table S5. **Paleointensity Values.**

Data Set S1. NRM AF Demagnetization data.

References

Crawford, D. A., and P. H. Schultz (1999), Electromagnetic properties of impact-generated plasma, vapor and debris, *Int. J. Impact Eng.*, *23*, 169-180, doi:10.1016/S0734-743X(99)00070-6.

Gattacceca, J., M. Boustie, L. Hood, J. P. Cuq-Lelandais, M. Fuller, N. Bezaeva, T. de Resseguier, and L. Berthe (2010), Can the lunar crust be magnetized by shock: Experimental groundtruth, *Earth Planet. Sci. Lett.*, *299*, 42-53, doi:10.1016/j.epsl.2010.08.011.

Grove, T. L., and D. Walker (1977), Cooling histories of Apollo 15 quartz-normative basalts, in *Proceedings of the Eighth Lunar Science Conference*, p. 1501-1520, Pergamon Press, Inc., New York.

Meyer, C. (2005), *Lunar sample compendium (online)*, 6, <http://curator.jsc.nasa.gov/Lunar/lsc/index.cfm>.

Renne, P. R., G. Balco, K. R. Ludwig, R. Mundil, and K. Min (2011), Response to the comment by WH Schwarz et al. on "Joint determination of ^{40}K decay constants and ^{40}Ar/^{40}K for the Fish Canyon sanidine standard, and improved accuracy for ^{40}Ar/^{39}Ar geochronology", *Geochim. Cosmochim. Acta*, *75*, 5097, doi:10.1016/j.gca.2011.06.021.

Renne, P. R., K. B. Knight, S. Nomade, K.-N. Leung, and T.-P. Lou (2005), Application of deuteron-deuteron (D-D) fusion neutrons to ^{40}Ar/^{39}Ar geochronology, *Applied Radiation and Isotopes*, *62*, 25-32, doi:10.1016/j.apradiso.2004.06.004.

Renne, P. R., C. C. Swisher, A. L. Deino, D. B. Karner, T. L. Owens, and D. J. DePaolo (1998), Intercalibration of standards, absolute ages and uncertainties in ^{40}Ar/^{39}Ar dating, *Chemical Geology*, *145*, 117-152, doi:10.1016/S0009-2541(97)00159-9.

Shea, E. K., B. P. Weiss, W. S. Cassata, D. L. Shuster, S. M. Tikoo, J. Gattacceca, T. L. Grove, and M. D. Fuller (2012), A long-lived lunar core dynamo, *Science*, *335*, 453-456, doi:10.1126/science.1215359.

Shuster, D. L., G. Balco, W. S. Cassata, V. A. Fernandes, I. Garrick-Bethell, and B. P. Weiss (2010), A record of impacts preserved in the lunar regolith, *Earth Planet. Sci. Lett.*, *290*, 155-165, doi:10.1016/j.epsl.2009.12.016.

Shuster, D. L., and W. S. Cassata (2015), Paleotemperatures at the lunar surfaces from open system behavior of cosmogenic ^{38}Ar and radiogenic ^{40}Ar, *Geochim. Cosmochim. Acta*, *155*, 154-171, doi:10.1016/j.gca.2015.01.037.

Steiger, R. H., and E. Jäger (1977), Subcommission on geochronology: convention on the use of decay constants in geo-and cosmochronology, *Earth Planet. Sci. Lett.*, *36*, 359-362, doi:10.1016/0012-821X(77)90060-7.

Tikoo, S. M., B. P. Weiss, J. Buz, E. A. Lima, E. K. Shea, G. Melo, and T. L. Grove (2012), Magnetic fidelity of mare basalts and implications for a lunar dynamo, *Earth Planet. Sci. Lett.*, *337-338*, 93-103, doi:10.1016/j.epsl.2012.05.024.

Turner, G. (1971), Argon 40- argon 39 dating: The optimization of irradiation parameters, *Earth Planet. Sci. Lett.*, *10*, 227-234, doi:10.1016/0012-821X(71)90010-0.